Title

Microglial pattern recognition via IL-33 promotes synaptic refinement in developing corticothalamic circuits in mice

Journal

Journal of Experimental Medicine, 220(2)

ISSN

0022-1007

Authors

Han, Rafael T
Vainchtein, Ilia D
Schlachetzki, Johannes CM
et al.

Publication Date

2023-02-06

DOI

10.1084/jem.20220605

Peer reviewed

JEM Journal of Experimental Medicine

ARTICLE

Microglial pattern recognition via IL-33 promotes synaptic refinement in developing corticothalamic circuits in mice

Rafael T. Han[1*], Ilia D. Vainchtein[1*], Johannes C.M. Schlachetzki[7], Frances S. Cho[2,3,6], Leah C. Dorman[1,2], Eunji Ahn[1], Dong Kyu Kim[1], Jerika J. Barron[1], Hiromi Nakao-Inoue[1], Ari B. Molofsky[4], Christopher K. Glass[7,8], Jeanne T. Paz[2,3,5,6], and Anna V. Molofsky[1,2,5]

Microglia are critical regulators of brain development that engulf synaptic proteins during postnatal synapse remodeling. However, the mechanisms through which microglia sense the brain environment are not well defined. Here, we characterized the regulatory program downstream of interleukin-33 (IL-33), a cytokine that promotes microglial synapse remodeling. Exposing the developing brain to a supraphysiological dose of IL-33 altered the microglial enhancer landscape and increased binding of stimulus-dependent transcription factors including AP-1/FOS. This induced a gene expression program enriched for the expression of pattern recognition receptors, including the scavenger receptor MARCO. CNS-specific deletion of IL-33 led to increased excitatory/inhibitory synaptic balance, spontaneous absence-like epileptiform activity in juvenile mice, and increased seizure susceptibility in response to chemoconvulsants. We found that MARCO promoted synapse engulfment, and *Marco*-deficient animals had excess thalamic excitatory synapses and increased seizure susceptibility. Taken together, these data define coordinated epigenetic and functional changes in microglia and uncover pattern recognition receptors as potential regulators of postnatal synaptic refinement.

Introduction

Innate immune signaling shapes tissue development and homeostasis, including the remodeling of neuronal synapses in the central nervous system (CNS). Immune dysfunction is also implicated in the pathogenesis of neurodevelopmental disorders, including epilepsy and schizophrenia (Bennett and Molofsky, 2019; Vezzani et al., 2015). Microglia, the dominant immune cells in the brain parenchyma, are exquisitely sensitive to environmental cues (Lavin et al., 2014; Hrvatin et al., 2018; Gosselin et al., 2014; Gosselin et al., 2017; Butovsky et al., 2014). This context sensitivity is thought to shape one of their dominant functions, which is to promote synapse remodeling in the developing brain (Mosser et al., 2017; Frost and Schafer, 2016). Mechanisms of microglial-mediated synaptic engulfment vary markedly by developmental stage and brain region (Faust et al., 2021) and are particularly sensitive to extracellular cues in later stages of synaptic refinement (~P10–P30 in the mouse). However, the molecular mechanisms through which microglia sense synaptic cues to promote remodeling are not well defined.

To investigate this question, we focused on the downstream signaling pathways orchestrated by the IL-1 family member interleukin-33 (IL-33), a recently described regulator of postnatal synapse refinement that acts via its obligate receptor (IL1RL1, a.k.a. ST2) expressed on microglia (Nguyen et al., 2020; Vainchtein et al., 2018; He et al., 2022). While these studies demonstrated IL-33–dependent engulfment of synaptic proteins in development and extracellular matrix proteins in the adult hippocampus, the molecular mechanisms involved and their impact on circuit maturation remain unknown. The somatosensory thalamus is one of the first brain regions to express IL-33, predominantly in astrocytes (Vainchtein et al., 2018), and its expression increases, coincident with synapse maturation in this region (Fig. 1 A; Golshani et al., 1998; Takeuchi et al., 2014;

[1]Departments of Psychiatry and Behavioral Sciences/Weill Institute for Neurosciences, University of California, San Francisco, San Francisco, CA, USA; [2]Neuroscience Graduate Program, University of California, San Francisco, San Francisco, CA, USA; [3]Department of Neurology, University of California, San Francisco, San Francisco, CA, USA; [4]Department of Laboratory Medicine, University of California, San Francisco, San Francisco, CA, USA; [5]Kavli Institute for Fundamental Neuroscience, University of California, San Francisco, San Francisco, CA, USA; [6]Gladstone Institute of Neurological Disease, San Francisco, CA, USA; [7]Department of Cellular and Molecular Medicine, University of California, San Diego, La Jolla, CA, USA; [8]Department of Medicine, University of California, San Diego, La Jolla, CA, USA.

*R.T. Han and I.D. Vainchtein contributed equally to this paper. Correspondence to Anna V. Molofsky: anna.molofsky@ucsf.edu; Rafael T. Han: rt.han@kist.re.kr

R.T. Han's current affiliation is Biomedical Research Division, Korea Institute of Science and Technology (KIST), Seoul, Republic of Korea. I.D. Vainchtein's current affiliation is Janssen Research & Development, San Diego, CA, USA.

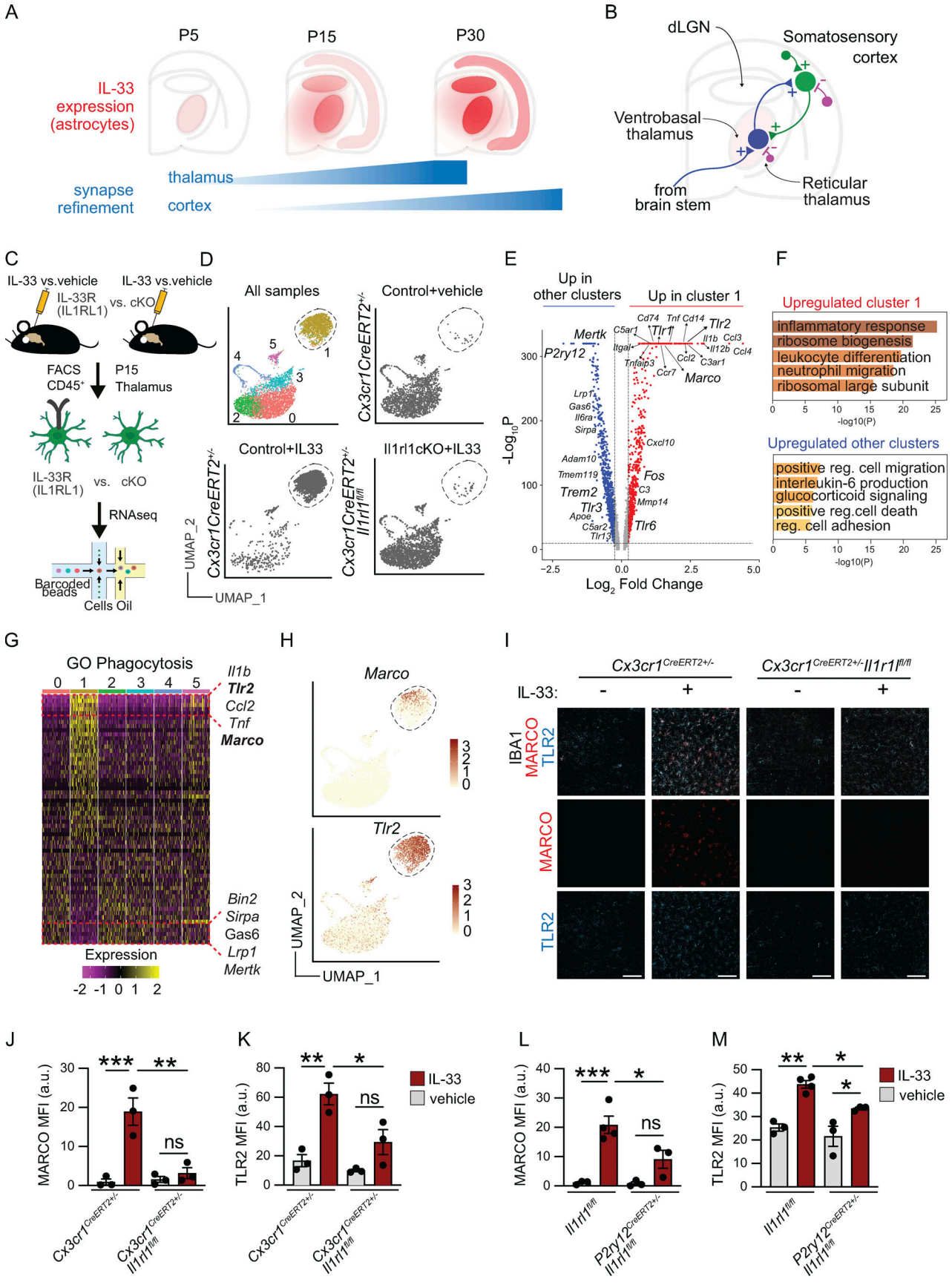

Figure 1. **IL-33 induces a phagocytic program in microglia that upregulates extracellular sensing and scavenging pathways. (A)** Schematic of developmental induction of IL-33 during corticothalamic synapse refinement (adapted from data in Vainchtein et al., 2018). **(B)** Circuit diagram of the

corticothalamic circuit, including excitatory thalamocortical (blue), corticothalamic (green), and inhibitory connections (violet). **(C)** Experimental paradigm for scRNA-seq from P15 thalamus (vehicle = PBS). **(D)** Unsupervised clustering of single-cell sequencing data from all three conditions (upper left). Same plot showing only *Cx3cr1*$^{CreERT2+/-}$ sample 4 h after vehicle injection (upper right), *Cx3cr1*$^{CreERT2+/-}$ sample 4 h after 40 ng IL-33 injection (lower left), and *Cx3cr1*$^{CreERT2+/-}$ *Il1rl1*$^{fl/fl}$ sample 4 h after 40 ng of IL-33 injection (lower right) plotted in UMAP space. Each dot represents a cell from one independent experiment. **(E)** Volcano plot of differentially expressed genes between the IL-33 responsive cluster 1 vs. aggregated cells from all other clusters. Red dots are upregulated in cluster 1 with $\log_2$ fold change >0.25, $p_{Adj} < 10^{-10}$, using the MAST test in Seurat. Blue dots are upregulated in all other aggregated clusters vs. cluster 1 with $\log_2$ fold change <0.25, $p_{Adj} < 10^{-10}$. **(F)** Top five GO terms upregulated in cluster 1 (upper) and upregulated in all other aggregated clusters (lower). **(G)** Heatmap showing expression of phagocytosis-related genes (GO: 0006909) across clusters, highlighting top five upregulated genes (top, yellow) and downregulated genes (bottom, purple) in cluster1 (ordered based on expression in cluster 1, centered normalized expression values). **(H)** Feature plots showing *Marco* (upper) and *Tlr2* (lower) expression with cluster 1 highlighted (dotted line). **(I)** Representative images of MARCO and TLR2 protein expression in thalamic microglia 18 h after vehicle or IL-33 injection in *Cx3cr1*$^{CreERT2+/-}$ or *Cx3cr1*$^{CreERT2+/-}$:*Il1rl1*$^{fl/fl}$ mice. Scale bar = 100 µm. **(J)** Quantification of MARCO mean fluorescence intensity (MFI) in thalamic microglia 18 h after vehicle or IL-33 injection in *Cx3cr1*$^{CreERT2+/-}$ or *Cx3cr1*$^{CreERT2+/-}$:*Il1rl1*$^{fl/fl}$ mice. Each dot represents a mouse. Two-way ANOVA followed by Tukey's post hoc comparison (genotype and treatment). **(K)** Quantification of TLR2 MFI in thalamic microglia 18 h after vehicle or IL-33 injection in *Cx3cr1*$^{CreERT2+/-}$ or *Cx3cr1*$^{CreERT2+/-}$:*Il1rl1*$^{fl/fl}$ mice. Each dot represents a mouse. Two-way ANOVA followed by Tukey's post hoc comparison (genotype and treatment). Data points represent the average of three technical repeats. **(L and M)** Quantification of MARCO (L) and TLR2 (M) expression in thalamic microglia 18 h after vehicle or IL-33 injection in *Il1rl1*$^{fl/fl}$ *or P2ry12*$^{creERT2+}$:*Il1rl1*$^{fl/fl}$ mice. Each dot represents a mouse. Two-way ANOVA followed by Tukey's post hoc comparison (genotype and treatment). Data points represent the average of two technical repeats. Data represented as mean ± SEM for bar graphs. Mice aged P15–P17 were used for I–M. dLGN: dorsal lateral geniculate nucleus of thalamus. *P < 0.05, **P < 0.01, ***P < 0.001.

Yoshida et al., 2009). Reciprocal connections between the somatosensory thalamus and cortex mature postnatally along a similar time course (Fig. 1 B; Midorikawa and Miyata, 2021). Hyperexcitability in these connections can drive absence seizures, a subtype associated with childhood absence epilepsy, the most common form of pediatric epilepsy (Crunelli et al., 2020). The robust expression of a microglial instructive cue during development raises the question of whether and how it shapes circuit maturation and function.

Here, we identify a coordinated set of epigenetic, transcriptomic, and functional changes in microglia that drive synapse engulfment in response to exogenous IL-33. We show that IL-33 induces the expression of pattern recognition and scavenger receptors by exposing enhancers that bind stimulus-dependent transcription factors, including FOS/AP-1. While not all of the targets identified may be relevant to IL-33's physiological roles in development, we identified the scavenger receptor MARCO as one downstream target of IL-33 signaling and demonstrated a role for MARCO in driving IL-33–dependent synaptic engulfment. We show that IL-33 controls excitatory/inhibitory synaptic balance in the developing thalamus and IL-33 deficiency leads to spontaneous absence seizures, a type of epilepsy associated with the corticothalamic circuit. Finally, we show that MARCO deficiency leads to impaired synaptic protein engulfment by microglia, excess excitatory synapses, and increased seizure susceptibility in juvenile animals. These data suggest a novel role for pattern recognition receptors in microglial synaptic remodeling.

Results

IL-33 induces a phagocytic program in microglia that upregulates pattern recognition and scavenging pathways

To define the IL-33–dependent phagocytic program, we performed single-cell sequencing of flow-sorted thalamic CD45$^+$ cells (predominantly microglia) 4 h after intracerebroventricular (i.c.v.) administration of recombinant IL-33 (40 ng, Fig. 1 C and Fig. S1 A). This dose and time period were chosen to capture the acute microglial response in a sufficient number of cells to detect transcriptomic shifts, and did not result in detectable infiltration of myeloid or lymphoid cells into the CNS (Fig. S1 B). However, this dose is likely much higher than what might be experienced in a physiological setting. To isolate direct effects on microglia, we conditionally deleted the IL-33 receptor *Il1rl1* on microglia (*Cx3cr1*$^{CreERT2+/-}$:*Il1rl1*$^{fl/fl}$ [Yona et al., 2013], tamoxifen: P1, P3, and P5) and compared it to the vehicle or IL-33–treated controls (*Cx3cr1*$^{CreERT2+/-}$). Unsupervised clustering revealed several distinct microglial clusters. (Fig. 1 D and Fig. S1 F, quality control in Fig. S1, C–E), including homeostatic (clusters 0 and 2, high *P2ry12*, *Mef2a*), proliferating (cluster 4, *Mki67*), interferon-responsive (cluster 5, *Ifitm3*, *Ifit3*), and a lysosomally/translationally active cluster (cluster 3, *Lyz2*, *Apoe*).

Most notable was a robust transcriptomic shift in 84% of microglia in response to IL-33 that was almost completely abrogated after microglial-specific deletion of the IL-33 receptor (Fig. 1 D). This "IL-33 responsive" cluster (1) expressed genes associated with "classical" macrophage activation, including *Tnf*, *Il1b*, and others (Fig. 1, E and F), many of which were concordant with genes we had identified as downregulated in microglia from IL-33–deficient animals (Vainchtein et al., 2018). These data demonstrate a direct effect of IL-33 on microglia and suggest that most microglia are competent to respond to IL-33.

To further explore IL-33 target genes that might have functional roles in phagocytosis, we overlaid our data with an annotated phagocytosis dataset (GO: 0006909). This revealed downregulation of some previously defined phagocytic genes, including *Trem2* (Shirotani et al., 2019; Filipello et al., 2018), and TAM receptor tyrosine kinase, *Mertk* (Fig. 1, E and G; Fourgeaud et al., 2016). In contrast, we observed robust induction of pattern recognition receptors (PRRs). This included the scavenger receptor *Marco* (Bowdish and Gordon, 2009), which has been implicated in debris clearance by dendritic cells and macrophages, as well as β-amyloid engulfment by microglia (Wilkinson and El Khoury, 2012; Xu et al., 2017). Another was *Tlr2* (Medzhitov and Janeway, 2000; Schaefer et al., 2005), which senses a variety of extracellular pathogens and damage-associated molecular patterns in complex with TLR1/6, both of which were also induced (Fig. 1, E and H).

We validated induction of both MARCO and TLR2 proteins after IL-33 exposure in vivo in the thalamus (Fig. 1, I–K and Fig. S1, I–L) and cortex (Fig. S1, G and H). This induction was abrogated after deletion of *Il1rl1* in microglia using *Cx3cr1*^{creER}. As *Cx3CR1*^{CreER} also targets border-associated macrophages and other myeloid cells, we phenocopied these results using *P2ry12*^{creER} (Fig. 1, L and M; *Il1rl1*$^{fl/fl}$ vs. *P2ry12*$^{creERT2+/-}$*Il1rl1*$^{fl/fl}$; tamoxifen at P2, P4, and P6), which is more specific to microglia (McKinsey et al., 2020) when compared to *Cx3cr1*^{creER}. In *P2ry12*^{creER}, *Il1rl1* deletion was more specific to microglia (Fig. S1, M–P), but somewhat less sensitive (~87–92% reduction in *Il1rl1* transcript, Fig. S1 Q). While it is possible that *P2ry12*^{creER} could target platelets, they are not thought to express *Il1rl1* (Rowley et al., 2011). Taken together, these data reveal that IL-33 signals microglia directly to induce a gene expression program that enhances microglial sensitivity to extracellular cues.

AP-1/FOS activation drives pattern recognition receptor expression in microglia

To determine potential transcriptional regulators responsible for this IL-33–dependent gene expression program, we next characterized the epigenetic changes in IL-33–exposed microglia using high-dose exogenous exposure and sorted cells 4 h after IL-33 injection (Fig. 2 A; gating in Fig. S1 A). We assessed chromatin accessibility using an assay for transposase-accessible chromatin sequencing (ATAC-seq; Buenrostro et al., 2013). We also performed chromatin immunoprecipitation sequencing for acetylation of histone H3 lysine 27 (H3K27ac ChIP-seq) to determine active regulatory regions (Creyghton et al., 2010). These data were cross-correlated with bulk RNA sequencing (bulk RNA-seq) performed in parallel, which was highly consistent with findings from single-cell RNA sequencing (scRNA-seq; Fig. S2, A and B; and Table S2).

Gene promoters are essential for initiation of transcription, but additional cell-type specific responses depend heavily on transcription factor (TF) binding to distal enhancer regions (Troutman et al., 2021). These enhancers are primed by lineage-determining TFs, such as PU.1, in macrophages. They are further regulated by stimulus-dependent TFs that respond to upstream receptor-mediated signaling, thus conferring sensitivity to environmental cues. Genome-wide comparisons of active chromatin regions with both ATAC-seq and H3K27ac peaks revealed that the injection of IL-33 robustly induced de novo enhancer peaks (≥3 kb upstream of the promoter; Fig. 2 B; quality control in Fig. S2, C and D). Most notable was the significant enrichment for binding sites of stimulus-dependent TFs, including AP-1 and NF-κB-p65 (Fig. 2 C and Table S3; Ruland, 2011; Thompson et al., 2009). There was a concomitant suppression of MEF2-binding sites associated with a microglial physiology/surveillance phenotype (Gosselin et al., 2014; Holtman et al., 2017). In contrast, the myeloid lineage–determining transcription factor PU.1 (Zaret, 2020) both gained and lost accessibility sites in response to IL-33, as found in other studies (Lau et al., 2020), which is consistent with the fact that pioneer factors such as PU.1 prime the binding of other transcription factors. Thus IL-33 increased accessibility to stimulus-dependent transcription factors, including the AP-1 transcription factor complex.

AP-1 is a heterodimeric complex that includes members of four families: Fos, Jun, ATF/CREB, and Maf (Gazon et al., 2018). *Fos* was the top TF induced after IL-33, and there was a significant induction of AP-1 family genes including *Batf*, *Junb*, and *Atf3* (Fig. 2 D). *Fos* is an immediate early gene typically associated with neuronal activation, but not commonly linked to microglia. To directly assess FOS occupancy at the de novo enhancers recruited by IL-33, we performed FOS ChIP-seq of microglia (gating strategy in Fig. S1 A). Representative examples of ATAC-seq (open), H3K27ac (active), and FOS ChIP-seq peaks from IL-33 vs. vehicle-exposed microglia are shown in the vicinity of *Marco* and *Tlr2* alongside mRNA levels in each condition (Fig. 2, E and F). Overall, we found that FOS occupied almost half (47.2%) of the IL-33 recruited enhancers, which putatively regulate 867 genes (Fig. 2 G). These data suggest that FOS/AP-1 is a major TF complex mediating IL-33 signaling in microglia.

To further validate whether microglial *Fos* induction occurs in vivo, we used Fos-TRAP2 to permanently label cells via *Fos*-dependent expression of tamoxifen-inducible Cre recombinase (Fig. 2 H; DeNardo et al., 2019). We found that IL-33 significantly increased the number (Fig. 2, I and J) and the percentage (Fig. S2, E and F) of FosTRAP$^+$ microglia. In contrast, the number of FosTRAP$^+$ neurons was unchanged, suggesting no effect of IL-33 on neuronal activation (Fig. 2 K). FosTRAP$^+$ microglia expressed significantly more TLR2 and MARCO protein relative to FosTRAP$^-$ microglia in the same sections (Fig. 2, L and M). Taken together, our data show that IL-33 enhances microglial sensitivity to stimulus-dependent transcription factors like FOS, and FOS induction correlates with target gene expression.

The scavenger receptor MARCO partly mediates microglial synapse engulfment and synapse elimination in response to exogenous IL-33

We previously demonstrated that local exogenous IL-33 drives increased microglial engulfment of synaptic proteins and a concomitant synapse depletion within 24 h (Vainchtein et al., 2018). We next investigated whether IL-33 downstream targets, including MARCO and TLR2, were causally implicated in these phenotypes. We quantified the engulfment of the presynaptic marker VGLUT1 using high-resolution confocal imaging and 3D reconstruction with the microglial reporter *Cx3cr1*^{GFP} (Jung et al., 2000). Injection of IL-33 increased VGLUT1 within CD68$^+$ microglial phagolysosomes, and this effect was significantly inhibited by coinjection of a MARCO function–blocking antibody (Fig. 3, A–C and Fig. S3 A; van der Laan et al., 1999; Pinheiro da Silva et al., 2007). To determine whether these effects on engulfment impacted overall synapse numbers, we quantified excitatory synapses after IL-33 exposure. We found a twofold reduction in excitatory synapses after IL-33 injection, as assessed by pseudocolocalization of pre- and postsynaptic proteins, VGLUT1 and HOMER1 (Ippolito and Eroglu, 2010), as well as examination of both pre- and postsynaptic puncta in isolation. This depletion was significantly attenuated with acute loss of function using α-MARCO antibodies in the thalamus (Fig. 3, D and E; and Fig. S3, B and C).

To validate these results with an independent approach, we quantified synapses in *Marco*$^{-/-}$ mice (model validation in Fig.

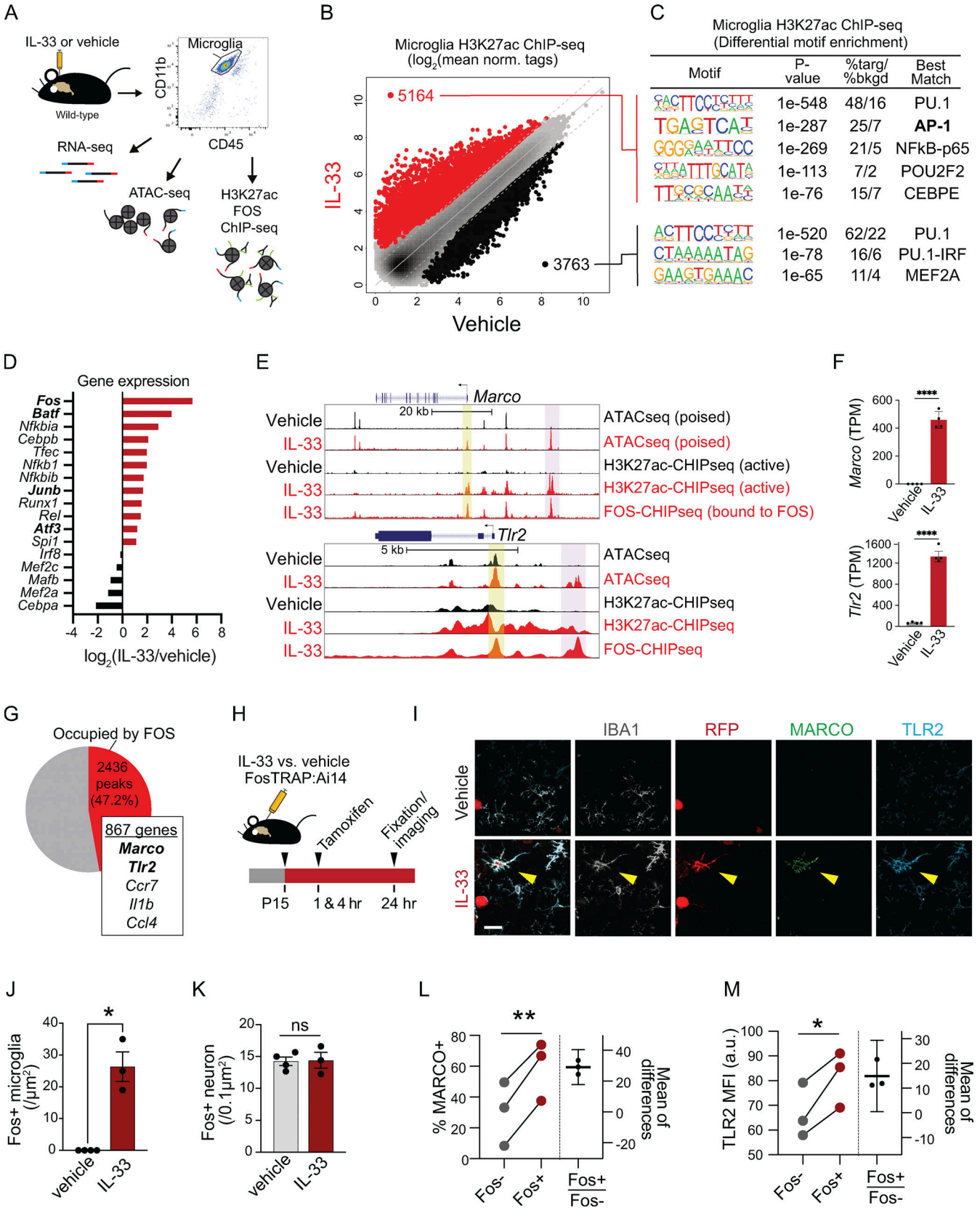

Figure 2. **AP-1/FOS activation drives pattern recognition receptor expression in microglia. (A)** Schematic of bulk RNA-seq, ATAC-seq, and H3K27ac/FOS ChIP-seq paradigm. Cells were collected 4 h after injection for analysis from one independent experiment. Vehicle = PBS. **(B)** Scatter plot of normalized H3K27ac ChIP-seq in regions with ATAC-seq signal, in microglia after vehicle or IL-33 exposure. Data focuses on putative enhancers (chromatin regions >3 kb from transcriptional start site). Colors indicate significant changes (FDR < 0.05 and FC > 2) in H3K27ac ChIP-seq signal (IL-33 enriched = red, vehicle enriched =

black). **(C)** Enriched de novo motifs in enhancers that gained or lost H3K27ac ChIP-seq signal after treatment with IL-33 or vehicle, showing best-matched TFs binding to those motifs. **(D)** Log_2 fold-change of gene expression of all transcription factors that bind DNA elements identified in C. All transcription factors shown have adj. P value < 0.001 by RNA-seq. **(E)** Browser tracks of ATAC-seq and H3K27ac or FOS ChIP-seq peaks in the vicinity of *Marco* and *Tlr2*. Yellow shading = promoter regions, pink shading = distal gene regulatory elements (enhancers). **(F)** Bar graphs illustrate mRNA expression (transcripts per million, TPM) from bulk RNA-seq for *Marco* and *Tlr2*. Error bars = standard deviation. Each dot represents a mouse (two-tailed unpaired *t* test). **(G)** Venn diagram depicting percentage of induced active open enhancer peaks occupied by FOS after IL-33. FOS-occupied enhancers putatively regulate 867 genes including *Marco* and *Tlr2*. **(H)** Experimental paradigm using the Fos-Trap2 allele crossed to the *Ai14* TdTomato reporter to label, or "trap" Fos + cells. Tamoxifen was administered 1 and 4 h after IL-33 or vehicle i.c.v. injection to capture Fos^+ cells, and animals were sacrificed 20 h after the last tamoxifen injection. **(I)** Representative images of staining for Fos-TRAP (TdT^+), MARCO, and TLR2 after vehicle or IL-33 injection. Scale bar = 10 µm. **(J)** Quantification of Fos^+ microglia in the cortex after vehicle or IL-33 injection. Dots = mice. **(K)** Quantification of Fos^+ neurons in the cortex after vehicle or IL-33 injection. Dots = mice. **(L)** Quantification of percent microglia that are $MARCO^+$ after IL-33 injection. Lines (left) connect paired measurements of Fos^+ and Fos^- microglia in the same mouse; estimation plot (right) shows the difference between the two means per mouse, error bars indicate 95% confidence interval. **(M)** Quantification of TLR2 mean fluorescent intensity after IL-33 injection. Lines (left) connect paired measurements of Fos^+ and Fos^- microglia in the same mouse. The estimation plot (right) shows the difference between the two means per mouse, error bars indicate 95% confidence interval. Data represented as mean ± SEM for J and K. Data points represent the average of two technical repeats for K–M. **(J and K)** Two-tailed unpaired *t* test. **(L and M)** Two tailed paired *t* = tests. Mice at P30 were used for A–G. *P < 0.05, **P < 0.01, ****P < 0.0001.

S3 D). We observed that supraphysiological local administration of IL-33 induced a twofold synapse depletion in the thalamus of wild-type animals (Fig. 3, F–H), whereas on a *Marco* deficient background the magnitude of this effect was diminished and was no longer statistically significant (Fig. 3, I–K). However, although a full comparison was not possible with this experimental design, we also noted that synapse numbers appeared to be increased in $Marco^{-/-}$ animals, suggesting that it might play physiological roles in brain development.

We also investigated whether TLR2, another potential downstream target of IL-33, impacted IL-33–dependent microglia synapse elimination. Acute blockade of TLR2 with a functional blocking antibody significantly impaired IL-33–dependent synapse engulfment by microglia (Fig. S3, E and F), but IL-33–mediated synapse depletion was not significantly attenuated on a *Tlr2*-deficient background (model validation in Fig. S3 D; and Fig. S3, G and H). Furthermore, a direct comparison of *Tlr2*-deficient animals and controls suggested a modest but nonsignificant trend toward excess excitatory synapses in $Tlr2^{-/-}$ mice (Fig. S3 I). Taken together, these data suggest that both TLR2 and MARCO can act downstream of exogenous IL-33 to promote excitatory synapse depletion but raise the possibility that MARCO might have physiological roles in the developing brain.

Loss of IL-33 signaling leads to excess corticothalamic excitatory synapses and spontaneous absence seizures

We next defined the functional impact of IL-33 on synaptic balance and excitability in the somatosensory circuit. During postnatal development, most IL-33–expressing cells in the cortex and thalamus are astrocytes, with a smaller contribution from oligodendrocytes (Fig. S4, A–C). We used *hGFAPcre* (Molofsky et al., 2014; Zhuo et al., 2001) to efficiently delete IL-33 throughout the brain ("IL-33 cKO," *hGFAPcre*:$Il33^{fl/fl}$ vs. $Il33^{fl/fl}$; Fig. S4 D). To quantify synapses, we focused on the reciprocal connections between the somatosensory cortex and thalamus, which include excitatory $VGLUT2^+$ sensory (lemniscal) afferents projecting from the brainstem, excitatory $VGLUT1^+$ cortical afferents, and $VGAT^+$ inhibitory synapses (Fig. 1 B). All of these synaptic connections mature during a period of rapid IL-33 increase in thalamic astrocytes, accelerating after the second postnatal week (Zolnik and Connors, 2016; Golshani et al., 1998; Yoshida et al., 2009).

We found a significant increase in the number of corticothalamic excitatory synapses (VGLUT1:Homer1) in IL-33 cKO animals vs. littermate controls (Fig. 4, A and B). The same effect was observed when examining pre- and postsynaptic proteins separately (Fig. S4, E and F). This was phenocopied with the loss of microglial IL-33R ($Cx3cr1^{CreERT2+/-}$:$Il1rl1^{fl/fl}$ vs. $Cx3cr1^{CreERT2+/-}$:$Il1rl1^{wt/wt}$; Fig. 4 C; and Fig. S4, G and H). We also observed an increase in brain stem afferent synapses in both genotypes (VGLUT2:Homer1; Fig. 4, D–F and Fig. S4, I–L). In contrast, the number of inhibitory synapses (VGAT:Gephyrin) in the somatosensory thalamus was significantly decreased in both genotypes (Fig. 4, G–I and Fig. S4, M–P). There were similar but more modest changes in synapse numbers in the somatosensory cortex of IL-33 cKO animals (Fig. S4, Q–S). We further validated these findings using whole-cell patch clamp electrophysiology of thalamic relay neurons (Fig. 4 J). We observed an increase in miniature excitatory postsynaptic currents (mEPSC; Fig. 4, K and L) and a reduction in miniature inhibitory postsynaptic currents (mIPSCs; Fig. 4, M and N). No changes in mEPSC/IPSC amplitude or kinetics were observed (Table S4). Taken together, these data support a model whereby local IL-33 acting directly on microglia promotes excitatory synapse elimination.

Hyperexcitability in the cortico-thalamo-cortical circuit can lead to seizures in rodent models (Huguenard and McCormick, 2007; Paz et al., 2013) and is associated with childhood absence epilepsy, one of the most common forms of pediatric epilepsy (Crunelli et al., 2020; Lüttjohann and van Luijtelaar, 2015). To investigate whether the increased excitation of corticothalamic excitatory circuits after the loss of CNS-derived IL-33 resulted in spontaneous seizures, we performed simultaneous video and electrocorticography (EcoG) recordings. Leads were placed in primary somatosensory (S1) and prefrontal (PFC) cortices and recording was performed in freely behaving juvenile mice (P35-P45; Fig. 4 O). 1 h of baseline recording in the home-cage environment revealed the presence of brief (1–3 s) spontaneous spike-wave discharges (SWDs) in 6/10 IL-33 cKO mice but in 0/8 littermate controls (Fig. 4, P and Q). These SWDs were frequently associated with behavioral arrest and observed simultaneously in both cortical regions (S1 and PFC), indicating that

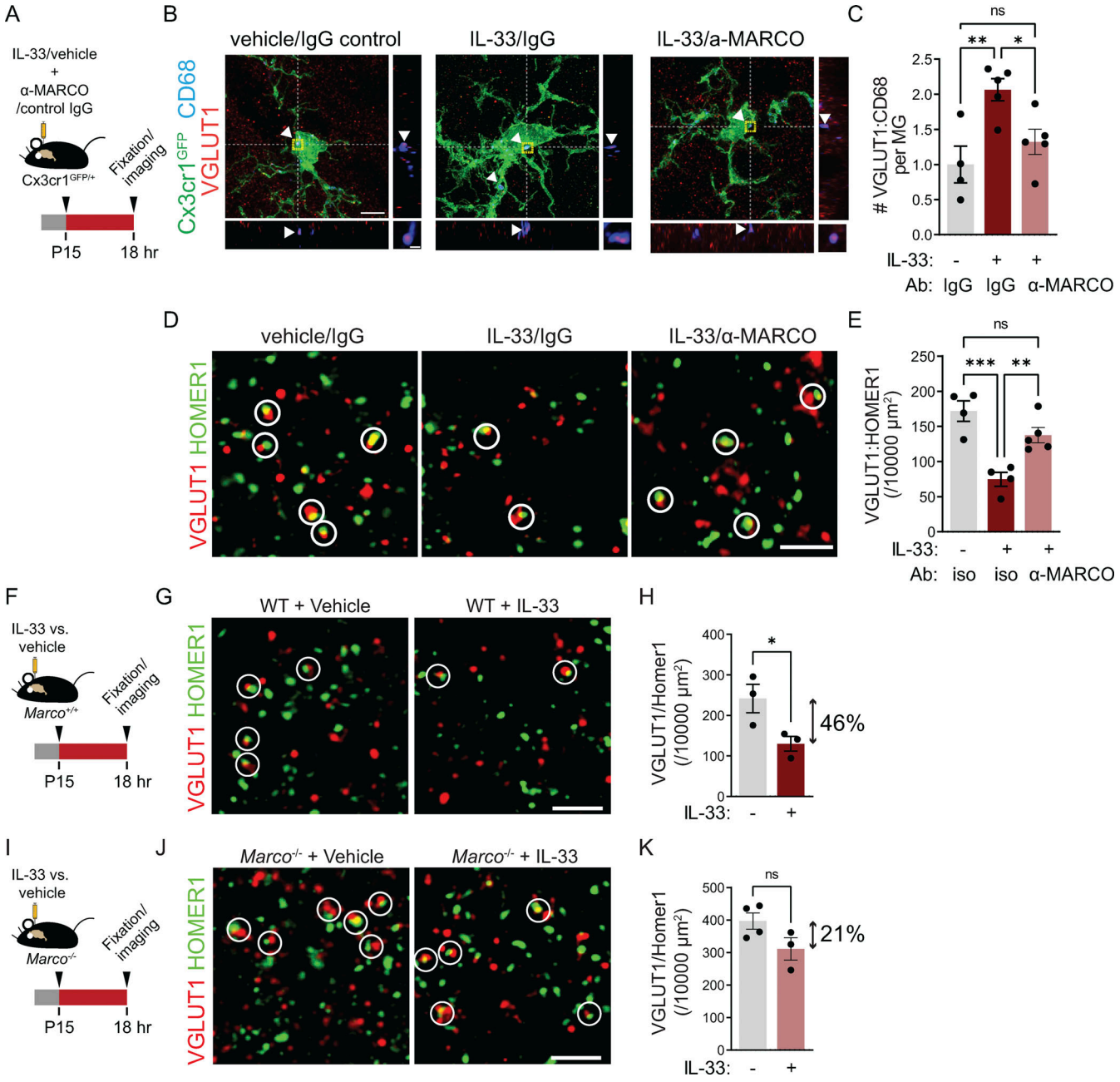

Figure 3. **The scavenger receptor MARCO partly mediates microglial synapse engulfment and synapse elimination in response to exogenous IL-33.** **(A)** Schematic of i.c.v. injection of IL-33 and MARCO-blocking antibody in *Cx3cr1*^{GFP} reporter animals. **(B)** Representative images of Z-stack maximum projection from *Cx3cr1*^{GFP} microglia in the somatosensory thalamus for the indicated conditions. Arrowheads and orthogonal projections highlight engulfed VGLUT1 within CD68$^+$ phagolysosomes. Vehicle = PBS. Scale bars = 5 µm (main panel) and 0.5 µm (inset). **(C)** Quantification of VGLUT1 within CD68$^+$ phagolysosomes within microglia 18 h after vehicle or IL-33 injection after co-injection of a MARCO-blocking antibody or isotype control (values normalized to vehicle + isotype control condition; *n* = 4 mice for vehicle + isotype control, *n* = 5 mice for IL-33 + isotype control and IL33 + MARCO blocking antibody). **(D and E)** Representative images and quantification of corticothalamic synapses in somatosensory thalamus 18 h after vehicle or IL-33 injection in the presence of MARCO blocking antibody or isotype control (*n* = 4 mice for vehicle + isotype control, *n* = 5 mice for IL-33 + isotype control and IL-33 + α-MARCO). Scale bar = 2 µm. **(F)** Schematic of i.c.v. injection of IL-33 in wild-type animals. **(G and H)** Representative images (G) and quantification (H) of corticothalamic excitatory synapses in somatosensory thalamus after vehicle or IL-33 injection into wild-type animals (*n* = 3 mice/condition). Scale bar = 2 µm. Two-tailed unpaired *t* test was used. Arrow indicates the magnitude of the difference between the two conditions. **(I)** Schematic of i.c.v. injection of IL-33 in *Marco*$^{-/-}$ animals. **(J and K)** Representative images (J) and quantification (K) of corticothalamic excitatory synapses in somatosensory thalamus after vehicle or IL-33 injection into *Marco*$^{-/-}$ animals (*n* = 4 mice for vehicle and 3 mice for IL-33). Scale bar = 2 µm. Two-tailed unpaired *t* test was used. Arrow indicates the magnitude of the difference between two conditions. Dots = individual mice. Data points represent the average of three technical repeats for all experiments. Mice aged P15–P17 used for all experiments. One-way ANOVA with Tukey's comparison was used for C and E. *P < 0.05, **P < 0.01, ***P < 0.001.

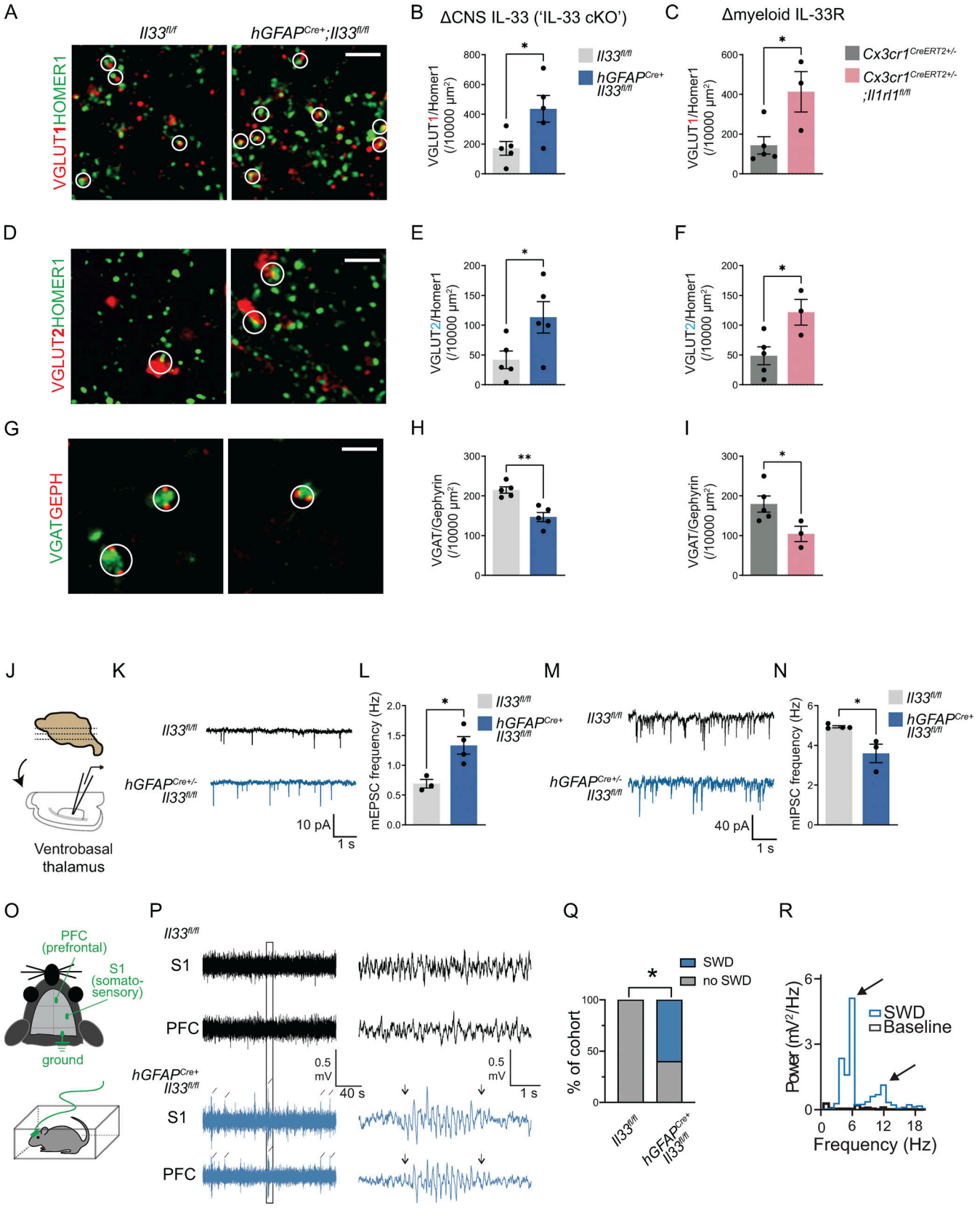

Figure 4. **Loss of IL-33 signaling leads to excess corticothalamic excitatory synapses and spontaneous absence seizures. (A)** Representative images of corticothalamic excitatory synapses within the ventrobasal thalamus as defined by colocalized presynaptic (VGLUT1) and postsynaptic (HOMER1) puncta in *hGFAP*$^{Cre+}$;*Il33*$^{fl/fl}$ vs. *Il33*$^{fl/fl}$ control. Circles indicate colocalization, defining a functional synapse. Scale bar = 2 µm. **(B)** Quantification of corticothalamic excitatory synapses in ventrobasal thalamus of *hGFAP*$^{Cre+}$;*Il33*$^{fl/fl}$ vs. *Il33*$^{fl/fl}$ control. *n* = 5 mice/genotype. **(C)** Quantification of corticothalamic excitatory synapses

in ventrobasal thalamus with myeloid-specific deletion of IL-33 receptor (*Cx3cr1Cre*$^{ERT2+/-}$;*Il1rl1*$^{fl/fl}$) vs. control (*Cx3cr1*$^{CreERT2+/-}$). *n* = 3 mice in *Cx3cr1*$^{CreERT2+/-}$;*Il1rl1*$^{fl/fl}$ and *n* = 5 mice in *Cx3cr1*$^{CreERT2+/-}$. **(D)** Representative images of brainstem afferent (lemniscal) synapses as defined by colocalized pre- (VGLUT2) and post- (HOMER1) synaptic puncta in *hGFAP*$^{Cre+}$;*Il33*$^{fl/fl}$ vs. *Il33*$^{fl/fl}$. Circles indicate colocalization, defining a functional synapse. Scale bar = 2 µm. **(E)** Quantification of brainstem afferent synapses in *hGFAP*$^{Cre+}$;*Il33*$^{fl/fl}$ vs. *Il33*$^{fl/fl}$ control mice. 5 mice/genotype. **(F)** Quantification of brainstem afferent synapses after myeloid-specific deletion of IL-33 receptor (*Cx3cr1Cre*$^{ERT2+/-}$;*Il1rl1*$^{fl/fl}$) vs. control (*Cx3cr1*$^{CreERT2+/-}$). *Cx3cr1*$^{CreERT2+/-}$;*Il1rl1*$^{fl/fl}$: *n* = 3 mice. *Cx3cr1Cre*$^{ERT2+/-}$: *n* = 5 mice. **(G)** Representative images of inhibitory synapses in ventrobasal thalamus as defined by colocalized presynaptic (VGAT) and postsynaptic (Gephyrin) puncta in *hGFAP*$^{Cre+}$;*Il33*$^{fl/fl}$ vs. *Il33*$^{fl/fl}$ control. Circles indicate co-localization, defining a functional synapse. Scale bar = 2 µm. **(H)** Quantification of thalamic inhibitory synapses in *hGFAP*$^{Cre+}$;*Il33*$^{fl/fl}$ vs. *Il33*$^{fl/fl}$ control. *n* = 5 mice/genotype. **(I)** Quantification of inhibitory synapses in ventrobasal thalamus in myeloid-specific deletion of IL-33 receptor (*Cx3cr1Cre*$^{ERT2+/-}$;*Il1rl1*$^{fl/fl}$) vs. control (*Cx3cr1*$^{CreERT2+/-}$). *Cx3cr1*$^{CreERT2+/-}$;*Il1rl1*$^{fl/fl}$: *n* = 3 mice. *Cx3cr1*$^{CreERT2+/-}$: *n* = 5 mice. **(J)** Experimental paradigm for whole cell patch-clamp electrophysiology of ventrobasal thalamic neurons. **(K)** Representative traces of mEPSC. **(L)** Quantification of mEPSC frequency in ventrobasal thalamic neurons (*Il33*$^{fl/fl}$ control: *n* = 17 neurons from three mice, *hGFAP*$^{Cre+}$;*Il33*$^{fl/fl}$: *n* = 18 neurons from four mice, two independent cohorts). **(M)** Representative traces of mIPSC. **(N)** Quantification of mIPSC frequency in ventrobasal thalamic neurons (*n* = 16 neurons from three mice in *Il33*$^{fl/fl}$, *n* = 17 neurons from three mice in *hGFAP*$^{Cre+}$;*Il33*$^{fl/fl}$, two independent cohorts). **(O)** Schematic of lead placement and setup for ECoG in 35–45-d-old mice. **(P)** Representative traces of recordings from somatosensory and prefrontal cortices of freely behaving mice. Diagonal lines indicate detected SWDs that were detected simultaneously in both cortical locations. Boxed area is enlarged to highlight a representative SWD lasting about 3 s, occurring in *hGFAP*$^{Cre+}$;*Il33*$^{fl/fl}$. Arrowheads indicate the beginning and end of the SWD event. **(Q)** Quantification of percent of cohort with SWDs. *n* = 10 *hGFAP*$^{Cre+}$;*Il33*$^{fl/fl}$ mice and 8 = *Il33*$^{fl/fl}$ mice from three independent experiments (Fisher's exact test). **(R)** Representative fast Fourier transform of an SWD observed in *hGFAP*$^{Cre+}$;*Il33*$^{fl/fl}$ mice. Note the peak at 4–6 Hz and a harmonic at 8–12 Hz. In all experiments, dots represent independent mice. Data points represent the average of two technical repeats for B, E, and H. Data points represent the average of three technical repeats for C, F, and I. Data in B–N are represented as mean ± SEM for bar graphs. Two-tailed unpaired *t* test used for A–N. P28–P35 mice were used for A–N. *P < 0.05, **P < 0.01.

they were bona fide events. SWD had a characteristic internal frequency of 4–6 Hz, with a harmonic peak at 8–12 Hz, clearly distinguishing them from sleep spindles (Fig. 4 R). These events were nonconvulsive and were not associated with an overall change in the baseline spectral density, which is consistent with the fact that spike-and-wave discharges are brief (Fig. S4, T and U). Taken together, we found that loss of IL-33 signaling led to absence-type seizures linked to alterations in cortico-thalamocortical circuit excitability.

Increased seizure susceptibility after the loss of CNS IL-33 or microglial IL-33 receptor

We next sought to determine whether susceptibility to convulsive seizures was also dependent on microglial IL-33 signaling. We performed EcoG recordings on control or IL-33 cKO animals after the injection of a chemoconvulsant, pentylenetetrazol (PTZ; 50 mg/kg), a $GABA_A$ receptor blocker (Fig. 5 A). We observed an increase in the frequency and amplitude of spikes in response to PTZ in IL-33 cKO vs. littermate controls in both somatosensory and PFC (Fig. 5, B–D; and Fig. S5, A and B). Consistent with this, after PTZ administration, EcoG recordings from IL-33 cKO mice showed higher power in the low frequency (delta frequency, 0.5–4 Hz) in both cortical regions over the 1-h recording period (Fig. S5, C and D).

We also quantified behavioral generalized tonic-clonic (GTC) seizures in independent cohorts of mice that had not undergone EcoG placement by video recording for 1 h after the injection of PTZ. Consistent with our EcoG findings, we observed an increased incidence of GTC seizures in IL-33 cKO animals in response to PTZ: 11/16 IL-33 cKO mice had at least one seizure compared with 3/15 littermate controls (Fig. 5, E and F). Increased c-Fos staining of IL-33 cKO animals after PTZ was consistent with these findings (Fig. S5, E and G). IL-33 cKO mice were also more susceptible to another chemoconvulsant—the glutamate receptor agonist kainic acid (Fig. S5, H and I).

The effect of IL-33 deficiency was phenocopied by deletion of the IL-33 receptor on microglia using two independent conditional deletion strategies. Mice with conditional deletion of IL-33R using Cx3cr1^{creER} had more seizures after PTZ injection than control littermates (Fig. 5 G; at least one seizure in 6/7 *Cx3cr1*$^{CreERT2+/-}$:*Il1rl1*$^{fl/fl}$ vs. 2/9 *Cx3cr1*$^{CreERT2+/-}$ littermate controls). We also observed a statistically significant effect after microglial-specific deletion of IL-33R using the P2ry12 ^{CreERT2} mouse line (Fig. 5 H; >1 seizure in 11/12 *P2ry12*$^{CreERT2+/-}$:*Il1rl1*$^{fl/fl}$ vs. 10/22 littermate *Il1rl1*$^{fl/fl}$). Taken together, these data show that brain-derived IL-33 signals directly through its receptor on microglia and restricts seizure susceptibility.

MARCO deficiency leads to impaired synaptic protein engulfment, excess excitatory synapses, and increased seizure susceptibility

To assess the functional relevance of MARCO as a physiological downstream target of IL-33 signaling, we directly investigated the effect of MARCO in the absence of exogenous IL-33 administration. To determine the impact of MARCO on microglial engulfment of synaptic proteins, we injected a MARCO function–blocking antibody into *Cx3cr1*^{GFP} reporter mice and quantified synaptic proteins within microglial lysosomes 18 h later. We observed significantly less VGLUT1 protein within microglial lysosomes after MARCO blockade compared with isotype controls (Fig. 6, A and B). We next quantified synapse numbers and found that as suggested by our data in Fig. 3, *Marco*$^{-/-}$ mice had significantly increased corticothalamic excitatory synapse numbers compared with controls (Fig. 6, C and D). Finally, we quantified seizure susceptibility in response to PTZ administration. We found that *Marco*$^{-/-}$ mice had an increased seizure susceptibility (Fig. 6, E and F; 9/16 *Marco*$^{-/-}$ vs. 3/21 littermate wild-type mice had more than one seizure after PTZ injection). In contrast, *Tlr2* deficiency, which had more modest impacts on synapses and synapse engulfment (Fig. S3), did not alter the seizure threshold (Fig. 6 G). Of note, given that these studies relied on measurements of seizure threshold, we cannot determine whether the seizure susceptibility in *Marco*-deficient animals is thalamocortical in origin. Taken together, these results indicate that the IL-33 target gene *Marco* restricts excitatory synapse numbers and limits seizure susceptibility.

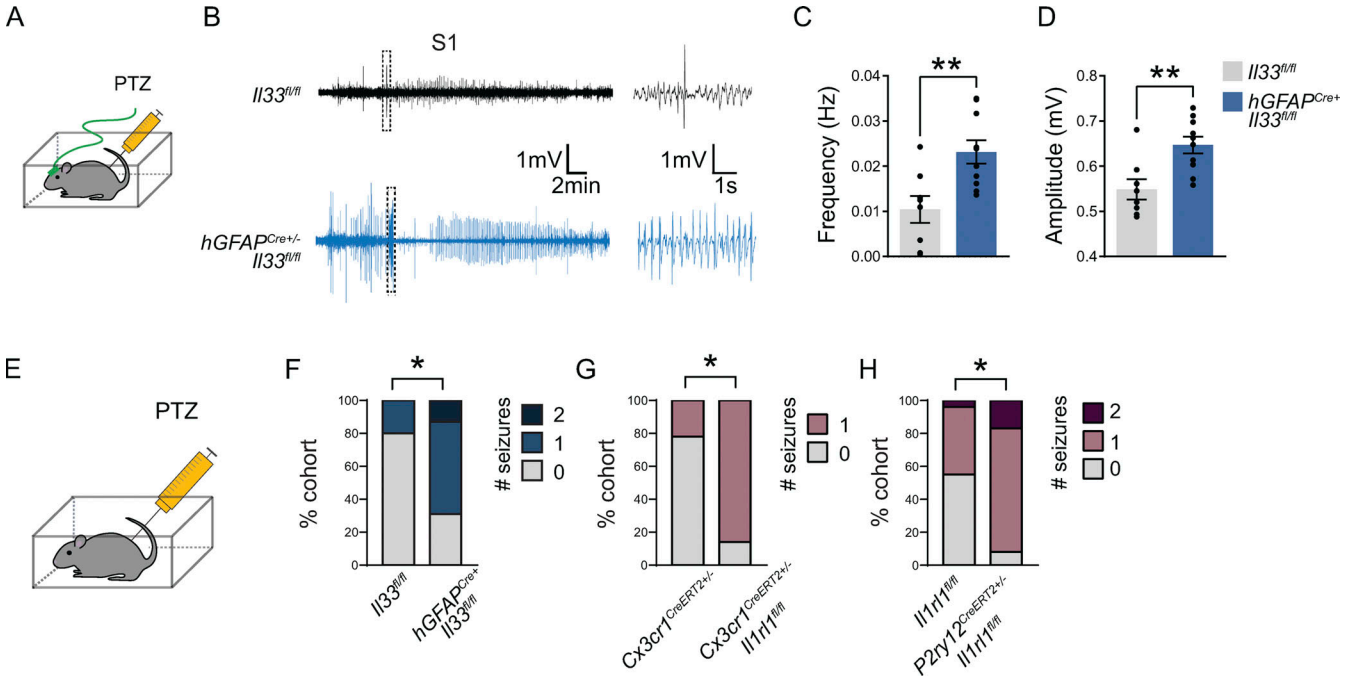

Figure 5. **Increased seizure susceptibility after the loss of CNS IL-33 or microglial IL-33 receptor. (A)** Schematic of ECoG recordings after injection of the GABA-A receptor antagonist PTZ. **(B)** Representative ECoG traces from the somatosensory cortex of PTZ-injected mice. Boxed area is enlarged to highlight epileptiform spikes (right). **(C and D)** Quantification of total spike frequency (C) and average amplitude (D) of detected ECoG spikes. n = 10 $hGFAP^{Cre+}$;$Il33^{fl/fl}$ mice and 8 $Il33^{fl/fl}$ mice from three independent experiments (35–45-d-old, two-tailed unpaired t test, mean ± SEM). **(E)** Schematic for seizure quantification after PTZ injection in non-implanted mice. **(F)** Percent of mice that experienced generalized tonic-clonic seizures during the 1-h recording. n = 16 $hGFAP^{Cre+}$; $Il33^{fl/fl}$ mice and 15 $Il33^{fl/fl}$, four independent experiments. Age P29–P35. Fisher's exact test. **(G)** Percent of mice that experienced generalized tonic-clonic seizures during the 1 h recording. n = 7 $Cx3cr1^{CreERT2+/-}$;$Il1rl1^{fl/fl}$ mice and n = 9 $Cx3cr1^{CreERT2+/-}$ mice, three independent experiments. Age P29–P35. Fisher's exact test. **(H)** Percent of mice that experienced generalized tonic-clonic seizures during the 1 h recording from n = 12 $P2ry12CreERT2^{+/-}$;$Il1rl1^{fl/fl}$ mice and n = 22 $Il1rl1^{fl/fl}$ mice, five independent experiments. Age P29–P35. Fisher's exact test. Dots represent individual mice. Data represented as mean ± SEM for bar graphs. ECoG, electrocorticography; S1, somatosensory cortex. *P < 0.05, **P < 0.01.

Discussion

Tissue-resident macrophages such as microglia are essential mediators of tissue remodeling and are optimized for tissue-specific functions by an exquisite sensitivity to local cues (Butovsky et al., 2014; Lavin et al., 2014; Gosselin et al., 2017; Ayata et al., 2018). Synapse remodeling is a brain-specific form of tissue remodeling and a dominant function of microglia in the developing brain. Here, we demonstrate that the tissue-resident cytokine IL-33 reprograms the microglial epigenome to expose enhancers that bind to stimulus-dependent TFs, including the AP-1/Fos complex.

In this study, we identified a microglial phagocytic program highly enriched for transmembrane pattern recognition receptors (PRRs), including TLR2 and the scavenger receptor MARCO (Bowdish and Gordon, 2009). We also found that MARCO had physiological roles in restricting excitatory synapse numbers and seizure susceptibility, whereas TLR2 did not. It is possible that these and many of the pathways identified in response to exogenous IL-33 may be relevant in the setting of injury, where IL-33 is known to function as an "alarmin" released in high doses after toxic cell death. However, in a physiological setting, our data also suggest that pattern recognition, such as by the scavenger receptor MARCO, can promote microglial phagocytosis. It raises the question of whether later stages of synapse refinement could be molecularly distinct from opsonin-mediated engulfment mechanisms, such as complement, that operate in earlier stages of development. Scavenger and pattern-recognition receptors have largely been studied in the context of host–pathogen interactions; thus the endogenous ligands for these receptors are not well understood. Future studies to identify the physiological ligands for microglial PRRs in the brain could provide an entry point to mechanistically define how microglia sense can remodel the synaptic space.

Finally, we demonstrate that both IL-33 and MARCO promote engulfment of excitatory synapses by microglia, restrict excitatory synapse numbers, and prevent hyperexcitability. More work needs to be done to fully define the mechanistic underpinnings of this hyperexcitability. For example, in this study and in previous work (Vainchtein et al., 2018), we consistently observed that IL-33 deficiency also led to a decrease in inhibitory synapses. The mechanisms for this effect remain to be determined, but it could result from homeostatic compensation at the neural circuit level, as can occur in mouse models of autism with altered excitatory/inhibitory (E/I) balance (Antoine et al., 2019). Future work will be needed to clarify this effect. Secondly, there are a variety of characteristic circuit changes associated with absence seizures that were not directly examined in this study, such as alterations in T-type calcium channels. Further, mechanistic dissection of how

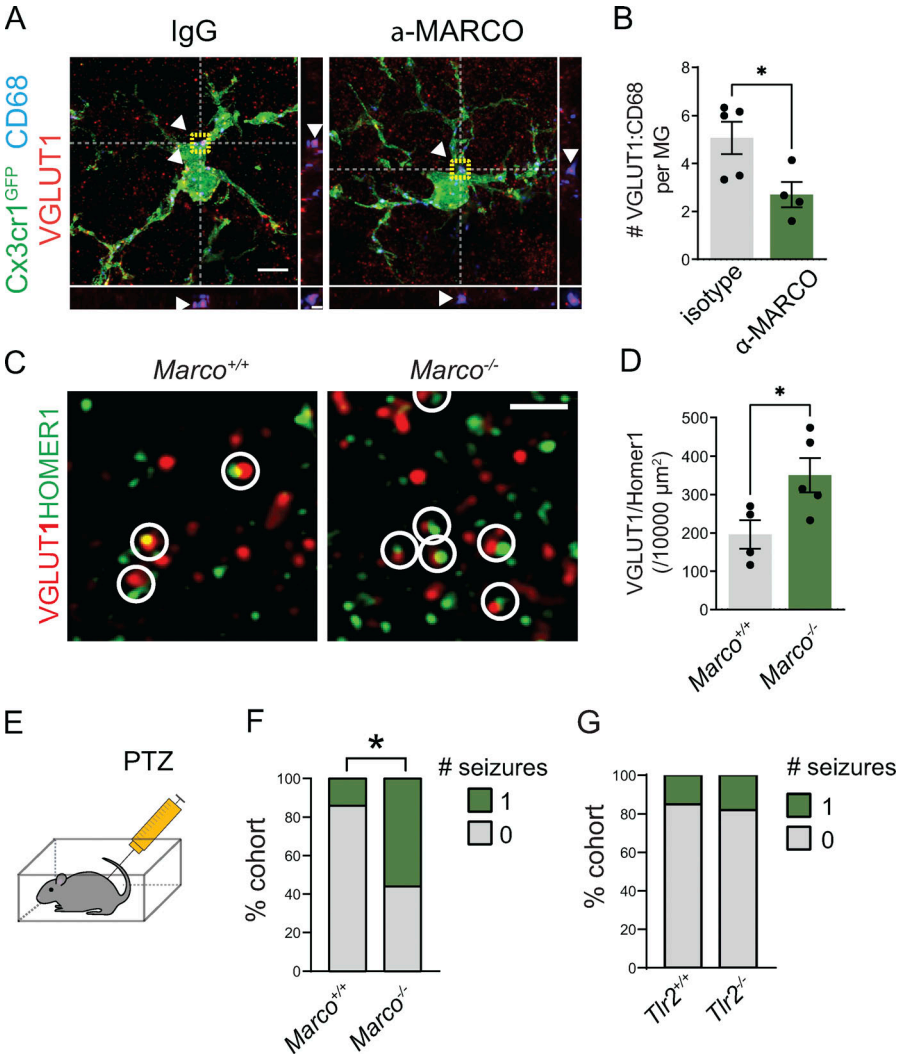

Figure 6. **MARCO deficiency leads to impaired synaptic protein engulfment, excess excitatory synapses, and increased seizure susceptibility. (A and B)** Representative image (A) and quantification (B) of VGLUT1 within CD68+ phagolysosomes within microglia 18 h after a MARCO-blocking antibody or isotype control at age P15–P16 (n = 5 mice for isotype control, n = 4 mice for MARCO-blocking antibody). Two-tailed unpaired t test. Scale bars = 5 µm (main panel) and 1 µm (inset). **(C and D)** Representative image (C) and quantification (D) of excitatory synapses in ventrobasal thalamus of *Marco*$^{+/+}$ and *Marco*$^{-/-}$ mice. *Marco*$^{+/+}$: n = 4 mice. *Marco*$^{-/-}$: n = 5 mice. Scale bar = 1 µm. Age P28–P30. Two-tailed unpaired t test. **(E)** Schematic for seizure quantification after PTZ injection. **(F)** Percent of mice that experienced generalized tonic-clonic seizures in 1 h after PTZ injection from n = 21 wild-type and 16 *Marco*$^{-/-}$ mice from four independent experiments. Age P29–P35. Fisher's exact test. **(G)** Percent of mice that experienced generalized tonic-clonic seizures in 1 h after PTZ injection from. n = 13 wild-type and 11 *Tlr2*$^{-/-}$ animals from two independent experiments. Age P28–P30. Fisher's exact test. In all bar graphs, dots represent independent mice. Data represented as mean ± SEM for bar graphs. *P < 0.05.

IL-33 and its downstream target MARCO promote a decrease in E/I balance will be necessary to determine if these pathways could have therapeutic relevance.

Neural circuit hyperexcitability is a phenotype thought to underly neurodevelopmental disorders including epilepsy, autism, and schizophrenia (Sohal and Rubenstein, 2019). Immune dysfunction has also been linked to these conditions through genetic, epidemiologic, and functional studies (Bennet and Molofsky, 2019). With the emergence of immunotherapies, microglia are increasingly attractive therapeutic targets. Our study defines a core pathway that restricts circuit hyperexcitability by regulating microglial phagocytic function, suggesting potential avenues toward immune-mediated therapies for neurodevelopmental disorders, such as childhood absence epilepsy.

Materials and methods

Resource table

Reagents and resources are listed in Table S5.

Contact for reagent and resource sharing

Anna Molofsky, anna.molofsky@ucsf.edu.

Experimental models and subject details

Mice

All mouse strains were maintained in the specific pathogen–free animal facility in University of California, San Francisco, and all animal protocols were approved by and in accordance with the guidelines established by the Institutional Animal Care and Use Committee and Laboratory Animal Resource Center. Littermate controls were used for all experiments when feasible, and all mice were backcrossed >10 generations on a C57BL/6 background unless otherwise indicated. The following mouse strains used are described in the table above and are as referenced in the text. For experiments using conditional alleles, Tamoxifen (T5648; Sigma-Aldrich) was diluted in corn oil (C8267; Sigma-Aldrich) at 37°C overnight and administered intragastrically at a concentration of 50 mg/kg three times every other day beginning at P1–P2 for Cx3cr1-creER and P2ry12-creER. 4-Hydroxytamoxifen (4-OHT; Hello Bio, HB6040) was dissolved at 20 mg/ml in ethanol by shaking at 37°C for 15 min and was then aliquoted and stored at −20°C for up to several weeks. Before use, 4-OHT was redissolved in ethanol by shaking at 37°C for 15 min, and corn oil (C8267; Sigma-Aldrich) was added to give a final concentration of 2.5 mg/ml 4-OHT. The final 2.5 mg/

ml 4-OHT solutions were always used on the day they were prepared and administered intraperitoneally at a concentration of 50 mg/kg.

Method details

Stereotaxic injections

All injections were performed with a Kopf stereotaxic apparatus (David Kopf Instruments) with a microdispensing pump (World Precision Instruments) holding a beveled glass needle with ∼50 µm outer diameter. For perinatal experiments, mice were anesthetized by hypothermia. For all postnatal (>P8) and adult injections, mice were anesthetized with 1.5% isoflurane at an oxygen flow rate of 1 liter/min, head-fixed with a stereotaxic frame, and treated with ophthalmic eye ointment. Fur was shaved and the incision site was sterilized with 70% ethanol and Betadine prior to surgical procedures. A hole was drilled in the skull. After injection, the glass pipette was left in place for several minutes to allow diffusion. The pipette was slowly removed and the scalp was reapposed with tissue glue. Body temperature was maintained throughout surgery using a heating pad. After surgery, Buprenorphine (Henry Schein Animal Health) was administered as needed by intraperitoneal injection at a concentration of 0.1 mg/kg. Further details for each experiment are given below.

Fos-TRAP2 labeling of Fos-expressing microglia

Homozygous Fos-TRAP2 mice (*Fos2A-CreER*) were crossed to R26R-lsl-TdTomato (*Ai14*) reporter mice. The heterozygous progenies for both alleles were administered 40 ng of recombinant IL-33 or vehicle (PBS) intracerebroventricularly as described separately. At 1 and 4 h after i.c.v. injection, mice were injected intraperitoneally with freshly prepared 4-OHT, a more rapidly bioavailable form of tamoxifen, at a concentration of 50 mg/kg. Mice were sacrificed 24 h after IL-33 i.c.v. injection. In a field of view, individual microglia IBA1 immunostaining was used to mask individual microglia, and Fos-CreER-Tdt positive and negative microglia were examined for TLR2 mean fluorescence intensity (as described separately) and the presence or absence of MARCO staining.

IL-33 and blocking antibody delivery

For bulk RNA-, ATAC-, and H3K27ac ChIP-seq, and quantitative RT-PCR, 500 ng of IL-33 or vehicle (PBS; 1 µl) was slowly injected (3–5 nl/s) into the right lateral ventricle (ML = 1.25 mm, AP = −0.6 mm, Z = −1.85 mm) of P30 mice. For all other experiments, including single-cell RNA-seq, in vivo microglia engulfment assay, in vivo microglia protein expression quantification, synapse counting, and FosTRAP2, either 40 ng of IL-33 or vehicle (PBS; 1 µl), was slowly injected (3–5 nl/s) into the right lateral ventricle (ML = 1.1 mm, AP = 3.5 mm from lambda, Z = −1.8 mm) of P14-P16 mice. For MARCO antibody blockade, 0.8 µg of MARCO antibody (Bio-Rad) or the same amount of IgG negative control antibody (MCA6004GA; Bio-Rad) was administered in the same needle with IL-33. For TLR2 antibody blockade, 1.6 µg of TLR2 antibody (InvivogGen) or the same amount of IgG negative control antibody (bgal-mab10-1; InvivogGen) was administered in the same needle with IL-33.

Quantification of mean fluorescence intensity of MARCO and TLR2

For in vivo microglia protein expression assay, mice were sacrificed 16–18 h after IL-33 i.c.v. injection. For quantification of MARCO and TLR2 intensity, a 4-µm-thick Z-stack image was obtained using an LSM 800 confocal microscope (Zeiss), and the maximum intensity projection image was created. Mean fluorescent intensity was quantified in ImageJ by first thresholding the Iba1 channel to make a mask for microglia soma and process, then measuring the intensity of MARCO and TLR2 channel in the masked area in a grey scale and averaging those values in a field of view. Default thresholding was used for Iba1 masking.

Fluorescence-activated cell sorting (FACS) of microglia

4 h after i.c.v. injection of IL-33 or vehicle (PBS), P30 mice were anesthetized with isoflurane and perfused with PBS. As described (Galatro et al., 2017), in brief, the brain was isolated and placed in ice-cold HBSS-Ca/Mg free supplemented with Hepes and glucose. The cortex was dissected and homogenized into a single-cell suspension using a tissue homogenizer (5 cm^3, VWR) and filtered through a 70-µm strainer (Falcon). Cells were pelleted at 300 × *g* for 10 min at 4°C and the supernatant was discarded. A 22% Percoll gradient was run on the pellet to deplete myelin at 900 × *g*, no brake at 4°C, and the pellet was afterward incubated with CD16/CD32 (eBioscience), CD11b-PE (eBioscience) or CD11b-APC (BioLegend), CD45-FITC (eBioscience) or CD45-APC (BioLegend), and Ly-6C-APC or Ly-6C APC/Cy7 (Biolegend) antibodies in HBSS-Ca/Mg free supplemented with Hepes, glucose, and EDTA (iMed-) on ice for 30 min. Cells were pelleted at 300 × *g* for 10 min at 4°C, resuspended in iMed- and incubated with DAPI just before FACS. A purified microglia population, defined as $CD11b^{high}CD45^{low}Ly\text{-}6C^{neg}$, was collected by FACS on a BD Aria3 (BD Biosciences). For scRNA-seq, a $CD45^+$ population was collected as shown in Fig. S1 A and processed further as described in 10× Genomics manual. For bulk RNA-seq and qPCR, microglia were lysed with RLT^+ (Qiagen) and stored at −80°C. For ATAC and H3K27ac ChIP-seq, microglia were processed as described below.

scRNA-seq of $CD45^+$ cells

After FACS, ∼10,000 $CD45^+$ cells were loaded into each well of a 10× Genomics Chromium Chip G (v3.1) and dual-index libraries were prepared as described in the 10× Genomics manual. Library quality was assessed by an Agilent High Sensitivity DNA kit on a Bioanalyzer (Agilent), and libraries were pooled and sequenced on Illumina NovaSeq SP100.

scRNA-seq analysis

Sequenced libraries were processed using the Cell Ranger 5.0 pipeline and aligned to the GRCm38 (mm10) mouse reference genome. Clustering and differential expression analysis were performed using Seurat version 4.0.1 (Satija et al., 2015; Hao et al., 2020 *Preprint*). Cells expressing <1,300 unique genes and 2,000 unique transcripts were excluded as likely debris, while cells expressing >5,000 genes or 20,000 transcripts were excluded to remove cell doublets. Cells with >5% mitochondrial transcripts were excluded to remove cells with membrane damage. Over 70% of the cells in each sample passed quality

control thresholding for a total of >2,000 cells per sample (*Cx3cr1*$^{creERT2+/-}$ + IL33 [Control + IL-33]: 2,205; *Cx3cr1*$^{creERT2+/-}$ + PBS [Control + Vehicle]: 2,730; and *Cx3cr1*$^{creERT2+/-}$:*Il1rl1*$^{fl/fl}$ + IL-33 [Il1rl1 cKO + IL33]: 2,707 healthy cells). An additional sample (*Cx3cr1*$^{creERT2+/-}$:*Il1rl1*$^{fl/fl}$ + Vehicle) was excluded because less than half of the 1,800 initially identified cells passed the quality control thresholds. Cells were identified as "female" or "male" based on their expression of the gene *Xist*; any cell expressing at least one count of *Xist* was labeled female, while all others were labeled male. The top seven transcripts correlated with sex (*Xist*, *Tsix*, *Ddx3y*, *Eif2s3y*, *Fkbp5*, *Ddit4*, and *Uty*) were identified using the VariancePartition (Hoffman and Schadt, 2016) package in R (1.20.0) and excluded from the PC, UMAP, and clustering calculations described below.

The top 6,000 most variable genes, excluding the seven sex-correlated genes above, were identified and their transcript counts normalized and scaled using the sctransform (Hafemeister and Satija, 2019) function in Seurat, regressing out percent mitochondrial RNA and total counts per cell. 50 principal components were calculated from the scaled genes. The Harmony package (1.0; Korsunsky et al., 2019) was used to adjust the top 50 PCs to reduce technical variability between samples. These adjusted PCs were used for the nearest neighbor, UMAP, and cluster identification. Cells were initially clustered with a resolution of 1, and two clusters (57 cells) with low expression of a canonical microglial gene (Cx3cr1) and nonzero expression of the myelin gene Mbp were excluded from downstream analysis due to likely nonmicroglial contamination. The remaining cells were then passed through all of the normalization and clustering steps described in this paragraph again. A clustering resolution of 0.4 was used to generate six clusters.

Differential expression (DE) analysis was done in Seurat using the MAST test (Finak et al., 2015) on the 6,000 most variable genes including only those genes expressed in at least 10% of the cells in a cluster. A P value was calculated only for genes with a fold change of 5% or more.

Heatmaps were created with the DoHeatmap function in Seurat including the top three genes by $\log_2$ fold change per cluster, including only genes with an adjusted P value < 10^{-9}. 100 randomly selected cells are shown per cluster. Feature and Dimensional UMAP plots show 2,000 cells per sample. For the phagocytosis gene-specific heatmap, phagocytosis genes were identified using the gene ontology (GO) term "Phagocytosis" (GO: 0006909), subset to include genes upregulated in cluster 1 by at least 7% (LFC > 0.1), and then ordered by descending log fold change in cluster 1. Only 100 cells are shown per cluster. GO analysis was performed using the Metascape webpage (Zhou et al., 2019; https://www.metascape.org), and only GO terms were used for Fig. 1 D.

Bulk RNA-seq of cortical microglia

RNA was isolated from 30,000 to 60,000 FACS-microglia per sample with the RNeasy Plus Micro kit (Qiagen). Quality and concentration were determined with the Agilent RNA 6000 Pico kit on a Bioanalyzer (Agilent). All samples had an RNA Integrity Number (RIN) >7. cDNA and libraries were made using the Ovation RNA-Seq System V2 kit (NuGen), and quality was assessed by Agilent High Sensitivity DNA kit on a Bioanalyzer (Agilent) and quantified by qPCR. Pooled libraries were RNA-sequenced on an Illumina HiSeq 4000 paired-end for 125 cycles (PE125) yielding 50–70 million reads per sample.

Bulk RNA-seq analysis

Read quality was assessed with FastQC (http://www.bioinformatics.babraham.ac.uk/projects/fastqc) and aligned to the Mus Musculus genome (Ensembl GRCm38) using STAR aligner (version 2.6.0; Dobin et al., 2013), with the additional command --outFilterMultimapNmax 1, to only keep reads that map one time to the reference genome. Aligned reads were counted using HTSeq (version 0.9.0; Anders et al., 2015), and the counts were loaded into R (The R Foundation). DESeq2 package (version 1.24.0; Love et al., 2014) was used to normalize the raw counts and perform differential gene expression analysis.

qPCR

RLT$^+$ (Qiagen) lysed microglia were vortexed and frozen at −80°C for storage. Samples were thawed and mRNA was isolated using RNeasy Plus Micro kit (Qiagen). Purified mRNA was converted to cDNA using the High Capacity cDNA Reverse Transcription kit (Life Technologies). Primers for *Hmbs*, *Rpsl7*, *Il1rl1*, and *Fos* were made using NCBI Primer Blast and ordered from IDT. A qPCR was run using Fast SYBR Green Master Mix (Thermo Fisher Scientific) on a 7900HT Fast Real-Time PCR System (Applied Biosystems). Data were analyzed using SDS software v2.4 (Applied Biosystems).

ATAC-seq of cortical microglia

Around 40,000–70,000 microglia were FACS-isolated and collected into iMed-. Cells were pelleted at 300 × *g*, 4°C. Afterward, a previously published protocol (Buenrostro et al., 2013) with modifications was used to perform ATAC-seq. In brief, the pellet was gently resuspended in ice-cold 50 µl lysis buffer (10 mM Tris-HCl, pH 7.4, 10 mM NaCl, 3 mM $MgCl_2$, and 0.1% IGEPAL CA-630) and spun down at 500 × *g* for 10 min and 4°C. The supernatant was discarded, and the cell pellet was gently resuspended in 20 µl of transposition reaction mix (10 µl tagment DNA buffer [Nextera, Illumina], 1 µl tagment DNA enzyme [Nextera, Illumina], and 9 µl nuclease free water) and incubated at 37°C for 30 min. Samples were stored at −20°C afterward. The next day, tagmented DNA was purified using MinElute PCR purification kit (Qiagen) and size-selected for 70—500 bp using AmpureXP beads (Beckman Coulter). Libraries were constructed and amplified using 1.25 µM Nextera index primers and NEBNext High-Fidelity 2× PCR Master Mix (New England BioLabs). A quantitative PCR was run to determine the optimal number of cycles. Libraries were afterward double-side selected with AmpureXP beads (Beckman Coulter) for 150–400 bp fragments and paired-end sequenced for 150 cycles (PE150) on an Illumina HiSeq 4000 yielding 40–60 million reads per sample.

ATAC-seq analysis

FASTQ files were mapped to the mouse mm10 genome (UCSC). Bowtie2 with default parameters was used to map ATAC-seq

experiments (Langmead and Salzberg, 2012). HOMER was used to convert aligned reads into "tag directories" for further analysis (Heinz et al., 2010). Peaks were called with HOMER for each tag directory with parameters -L 0 -C 0 -fdr 0.9 -minDist 200 -size 200. IDR was used to test for reproducibility between replicates, and only peaks with IDR < 0.05 were used for downstream analysis. The pooled tag directory from four replicates was used to track visualization using the UCSC genome browser (Kent et al., 2002). To quantify chromatin accessibility, peak files were merged with HOMER's mergePeaks and annotated with raw tag counts with HOMER's annotatePeaks using parameters -noadj, -size given. DESeq2 (Love et al., 2014) was used to identify chromatin accessibility with greater than two-fold change and adj. P value < 0.05. Motif enrichment was performed using HOMER's motif analysis (findMotifsGenome.pl), and de novo motifs were used. The background sequences were from the comparing condition as indicated in the figure legends.

H3K27ac chromatin immunoprecipitation-sequencing (H3K27ac ChIP-seq)

ChIP for H3K27ac was performed essentially as described previously (Nott et al., 2019). In brief, FACS-purified cells were fixed with 1% formaldehyde for 10 min at room temperature. Next, formaldehyde was quenched with 2.625 M glycine for 5 min at room temperature. Cells were collected by centrifugation at 1,500 × *g* for 10 min at 4°C. Cell pellets were then snap-frozen and stored at −80°C. For ChIP reactions, cell pellets were thawed on ice and lysed in 130 µl LB3 (10 mM Tris/HCl, pH 7.5, 100 mM NaCl, 1 mM EDTA, 0.5 mM EGTA, 0.1% deoxycholate, 0.5% sarkosyl, 1× protease inhibitor cocktail, and 1 mM sodium butyrate). Samples were sonicated in a 96-Place microTUBE Rack (cat# 500282; Covaris) using a Covaris E220 for 12 cycles with the following setting: time 60 s; duty 5.0; PIP, 140; cycles, 200; and amplitude/velocity/dwell 0.0. Samples were collected and 10% Triton X-100 was added to 1% final concentration. Sonicated samples were spun down at max speed, 4°C for 10 min. 1% of the sonicated lysate was saved as a ChIP input. The sonicated lysate was added to 20 µl Dynabeads Protein A with 1.5 ug anti-H3K27ac (Active Motif, #39685 Mouse Monoclonal) and incubated with slow rotation at 4°C overnight. The following day, beads were collected using a magnet and washed three times each with ice-cold wash buffer I (20 mM Tris/HCl, pH 7.5, 150 mM NaCl, 1% Triton X-100, 0.1% SDS, 2 mM EDTA, and 1× protease inhibitor cocktail) and ice cold wash buffer III (10 mM Tris/HCl, pH 7.5, 250 mM LiCl, 1% Triton X-100, 0.7% deoxycholate, 1 mM EDTA, and 1× protease inhibitor cocktail). Beads were then washed twice with ice-cold 10 mM Tris/HCl, pH 7.5, 1 mM EDTA, and 0.2% Tween-20. Sequencing libraries were prepared for ChIP products while bound to the Dynabeads Protein A initially suspended in 25 µl 10 mM Tris/HCl, pH 8.0, and 0.05% Tween-20.

ChIP libraries were prepared while bound to Dynabeads using NEBNext Ultra II Library preparation kit with reaction volumes reduced by half, essentially, as previously described (Heinz et al., 2010). Libraries were eluted and crosslinked-reversed by adding to the 46.5 µl NEB reaction a mastermix containing 20 µl water, 4 µl 10% SDS, 4.5 µl of 5 M NaCl, 3 µl of 0.5 M EDTA, and 1 µl of 20 mg/ml proteinase K, followed by incubation at 55°C for 1 h and 65°C overnight in a thermal cycler. Dynabeads were removed from the library using a magnet and the libraries were cleaned by adding 2 µl SpeedBeads 3 EDAC in 61 µl 20% PEG8000/1.5 M NaCl, mixing well, then incubating at room temperature for 10 min. SpeedBeads were collected on a magnet and washed two times with 150 µl 80% ethanol for 30 s. Beads were collected and ethanol was removed following each wash. After the second ethanol wash, beads were air-dried and DNA eluted in 25 µl 10 mM Tris/HCl, pH 8.0, and 0.05% Tween-20. DNA was amplified by PCR for 14 cycles in a 50 ml reaction volume using NEBNext Ultra II PCR master mix and 0.5 mM each Solexa 1GA and Solexa 1GB primers. Libraries were cleaned up as described above using 2 µl SpeedBeads and 36.5 µl 20% PEG 8000/1.5 M NaCl and 2 µl SpeedBeads. After ethanol washing and drying, PCR-amplified libraries were eluted from the SpeedBeads using 20 µl 10 mM Tris/HCl, pH 8.0, and 0.05% Tween-20. Next, the libraries were size-selected as 200–500 bp using gel extraction using 10% TBE acrylamide gels. Libraries were single-end sequenced for 50 cycles (SE50) using an Illumina HiSeq4000.

FOS ChIP-seq

ChIP for FOS used a previously described protocol for transcription factors (Texari et al., 2021) with slight modifications. In brief, the cell suspension was fixed in 2 mM disuccinimidyl glutarate (DSG/PBS; Thermo Fisher Scientific) for 30 min at RT on a shaker followed by 1% formaldehyde for 10 min at RT. The fixation was quenched with 1/20th volume 2.625 M glycine and 1/20th volume 10% BSA for 5 min at RT. Cell pellets were collected by centrifugation at 1,000 × *g* for 10 min at 4°C. Cell pellets were incubated with antibodies in 0.5% BSA/PBS, as described above for FACS. FACS-collected microglia were spun down at 1,000 × *g* for 10 min at 4°C and cell pellets were snap-frozen in dry ice with ethanol and stored at −80°C. For ChIP reactions, cell pellets were thawed on ice and lysed in 1 ml ice-cold resuspension buffer (9 mM Hepes-KOH, pH 7.9, 80 mM KCL, 0.9 mM EDTA, 0.5% IGEPAL CA-630, 1× protease inhibitor cocktail, and 1× Phenylmethylsulfonyl fluoride). Cells were pelleted at 1,000 × *g* for 5 min at 4°C. The pellet was resuspended in 80 µl ice-cold lysis buffer (20 mM Tris/HCl, pH 7.5, 150 mM NaCl, 1 mM EDTA, 0.5 mM EGTA, 0.4% deoxycholate, 0.1% SDS, 1% IGEPAL CA-630, 0.5 mM DTT, 1× protease inhibitor cocktail, and 1× phenylmethylsulfonyl fluoride) and the lysate transferred to Covaris sonication tubes on ice. Tubes were sonicated on a Covaris S2 with the following settings: intensity: 4W, duty cycle: 5%, cycles/burst: 200, time: 18 min (18 cycles at 60 s). The sonicated chromatin was transferred to 1.5 ml DNA loBind tubes and centrifuged at 16,000 × *g* at 4°C. The supernatant was transferred to PCR 0.2 ml tubes and 3% was set aside as the ChIP-input. 100 µl of lysis buffer with protein A Dynabeads (20 µl per sample) bound with FOS (1:50, 9F6; Cell Signaling Technology) was added and the tubes were rotated overnight (up to 16 h) at 4°C with gentle rotation. Tubes were placed on a magnetic plate, washed two times with lysis buffer, washed six times with ChIP wash buffer (10 mM Tris/HCl, pH 7.5, 250 mM LiCl, 0.5%

IGEPAL CA-630, 1 mM EDTA, 0.7% sodium deoxycholate, and 0.5× PIC), washed three times with TET (10 mM Tris/HCl, pH 8.0, 1 mM EDTA, 0.2% Tween 20, and 0.5× PIC), and washed one time with low EDTA TE (10 mM Tris/HCl, pH 8.0, 0.1 mM EDTA, and 0.5× PIC) and then collected in TT (10 mM Tris/HCl pH 8.0, and 0.05% Tween 20). Both ChIP-inputs and ChIP samples were diluted up to 46.5 µl with UltraPure Water and 29 µl of buffer (1.4% SDS, 50 mM EDTA, 30 mM EGTA, 20 µg Proteinase K, and 10 µg RNase A in UltraPure water) followed by addition of 4.5 µl of 5 M NaCl. The samples were gently mixed and incubated at 55°C for 1 h followed by 65°C for 10 h. DNA was purified using a double-sided selection using AmpureXP beads (Beckman Coulter) for 200–800 bp sizes.

ChIP DNA from ChIP input and ChIP samples was used to prepare libraries using the NEBNext Ultra II Library preparation kit (#E7645S) and NEBNext Multiplex Oligos for Illumina (Index Primers Set 1; #E7335S) according to manufacturer's protocol. Libraries were amplified by PCR for 12 cycles. Libraries were afterward double-side selected with AmpureXP beads (Beckman Coulter) for 150–400 bp fragments and single-end sequenced for 65 cycles (SE65) on an Illumina HiSeq 4000 yielding 40–50 million reads per sample.

ChIP-seq analysis

For preprocessing, Bowtie2 with default parameters was used to map ATAC-seq and ChIP-seq experiments (Langmead and Salzberg, 2012). HOMER was used to convert aligned reads into tag directories for further analysis (Heinz et al., 2010). To quantify H3K27ac signal, peak files were merged with HOMER's mergePeaks and quantified with raw tag counts with HOMER's annotatePeaks using parameters -noadj -size 1,000 -pc 3 on ATAC-associated peaks. ChIP peak signals were normalized to the sequencing depth. Peaks that contained at least four tags in at least one sample were used to identify differentially bounded peaks (FC > 2 and P adj <0.05) by DESeq2 (Love et al., 2014). Distal peaks that are ≥3 kb away from known TSS were categorized as enhancer peaks.

Motif enrichment

To identify de novo motifs enriched in enhancer peak regions over a random genomic background, HOMER's motif analysis (findMotifsGenome.pl) was used. We performed a de novo motif analysis on H3K27ac signal within 300 bp of ATAC-associated peaks. In addition, ATAC enhancer peaks anchored onto the H3K27ac signal were overlayed with FOS-occupied enhancer peaks to calculate the percentage of overlap. Overlapping peaks were annotated with HOMER's annotatePeaks and the number of associated genes was calculated. Genes with multiple enhancers were counted as one gene. The UCSC genome browser (Kent et al., 2002) was used to visualize ChIP-seq and ATAC-seq data.

Mouse immunohistochemistry

Mice were perfused transcardially with ∼10 ml of ice-cold 1X PBS followed by ∼10 ml of 4% paraformaldehyde (PFA) diluted in PBS. Brains were postfixed in 4% PFA for a minimum of 3 h and then transferred to a 30% sucrose solution until they were fully submerged. Brains were then embedded in OCT compounds, frozen, and sliced into 14-µm thick coronal sections on a CryoStar NX70 Cryostat (Thermo Fisher Scientific). Brain sections were incubated in a blocking solution consisting of 5% normal goat serum (Thermo Fisher Scientific) and 0.4% Triton X-100 (Sigma-Aldrich) diluted in 1X PBS for 1 h. Primary staining was done in the same blocking solution overnight at 4°C. Secondary antibodies were diluted in the same blocking solution, and tissue was incubated for 45 min at room temperature. Brain sections were mounted on coverslips with DAPI Fluoromount-G (0100-20; SouthernBiotech) for all other experiments. Histology slides were imaged on an LSM780 or LSM800 or LSM880 confocal microscope with AiryScan (Zeiss) on Superresolution mode using a 63× objective for synapse quantification and microglia engulfment assay, and an LSM 700 or LSM 800 confocal microscope (Zeiss) using 20× objective was used for all other imaging. The following goat secondary antibodies and their dilutions were used corresponding to the host of primary antibodies: Alexa Fluor 405 (1:500; Abcam), Alexa Fluor 488, Alexa Fluor 555, and Alexa Fluor 647 (1:500; Thermo Fisher Scientific).

Western blotting

Tissues were flash-frozen on dry ice and then sonicated for 20 s in lysis buffer (50 mM Tris-HCl, 1 mM EDTA, 1% Tx-100, and 150 mM NaCl). The sample was centrifuged for 10 min at 15,000 rpm at 4°C and the pellet was discarded. Samples were run on a denaturing gel and transferred to PVDF membrane, blocked with 5% milk in TBST for 1 h at room temperature, incubated in primary antibody overnight at 4°C and secondary antibody at room temperature for 1 h, and developed with ECL plus. The following secondary antibodies and their dilutions were used: rabbit anti-goat HRP-linked secondary (1:1,000, 1721034; Bio-Rad) and goat anti-rabbit HRP-linked secondary (1:2,000, 7074S; Cell Signaling Technology).

Slice preparation

Slices were prepared as previously described (Nguyen et al., 2020). Briefly, we prepared 250-µm-thick horizontal slices including thalamus in ice-cold sucrose cutting solution containing 234 mM sucrose, 2.5 mM KCl, 1.25 mM NaH_2PO_4, 10 mM $MgSO_4$, 0.5 mM $CaCl_2$, 26 mM $NaHCO_3$, and 10 mM glucose, equilibrated with 95% O_2 and 5% CO_2, pH 7.4, using a Leica VT1200 vibrating microtome (Leica Microsystems) from 4-mo-old mice. We incubated the thalamic slices, initially at 32–34°C, for an hour and then at room temperature in artificial cerebrospinal fluid containing 126 mM NaCl, 2.5 mM KCl, 1.25 mM NaH_2PO_4, 1 mM $MgCl_2$, 2 mM $CaCl_2$, 26 mM $NaHCO_3$, and 10 mM glucose, equilibrated with 95% O_2 and 5% CO_2, pH 7.4.

Whole-cell patch-clamp recording

Recordings were performed as described (Nguyen et al., 2020). Briefly, recording electrodes made of borosilicate glass had a resistance 3–5 MΩ when filled with intracellular solution containing 115 mM potassium gluconate, 11 mM KCl, 1 mM $MgCl_2$, 1 mM $CaCl_2$, 10 mM Hepes, and 11 mM EGTA, 2 mM K_2ATP, 0.1% biocytin, pH adjusted to 7.35 with KOH (286 mOsm) for mEPSCs recording or 129 mM CsCl, 5 mM QX-314Cl, 2 mM $MgCl_2$, 10 mM Hepes, and 10 mM EGTA, 4mM MgATP, 0.1% biocytin, pH

adjusted to 7.38 with CsOH (288 mOsm) for inhibitory postsynaptic currents (mIPSCs) recording. Series resistance was monitored in all recordings, and the recordings were excluded from analysis if the series resistance was >25 MΩ or varied by >20%. Recordings were obtained using a MultiClamp 700B (Molecular Devices), digitized (Digidata 1550B; Molecular Devices), and acquired at 20 kHz using the pClamp 10 software (Molecular Devices). Recordings were performed in a voltage-clamp mode at a holding potential of −70 mV and obtained from visually identified neurons in the somatosensory thalamus for 10 min. In the presence of 0.5 µM tetrodotoxin, 50 µM picrotoxin (P1675; Sigma-Aldrich) or 50 µM D-(−)-2-amino-5-phosphonopentanoic acid (5AP; HB0225; Hello Bio) and 20 µM 6,7-Dinitroquinoxaline-2,3(1H,4H)-dione (DNQX, D0540; Sigma-Aldrich) were used to isolate mEPSCs or mIPSCs, respectively. The recordings were analyzed using ClampFit (Molecular Devices) and MiniAnalysis (Synaptosoft).

Microglial engulfment assays

For the quantification of in vivo microglial synapse engulfment, 16–18 h after i.c.v. injection of IL-33 or vehicle (PBS) and MARCO/TLR2 antibody or IgG negative control antibody, the brains were postfixed in 4% PFA for a minimum of 6 h and transferred to a 30% sucrose solution until they were fully submerged. The brains were cut in 30-µm thick horizontal sections using HM 440E freezing microtome (GMI Instruments).

Quantification of engulfment was performed as previously described (Vainchtein et al., 2018). Briefly, Z-stacks encompassing entire microglia were collected with a Zeiss LSM880 confocal microscope with AiryScan (Zeiss) on Superresolution mode (~150 nm resolution) using a 63× objective with NA 1.4. Laser power and gain were consistent across all experiments. Images were analyzed using Imaris software (Bitplane) by creating a 3D surface rendering of microglia, thresholded in pilot experiments to ensure that microglial processes were accurately reconstructed and maintained consistently thereafter. This rendering of microglia was used to mask the CD68 channel to create a 3D surface rendering of phagolysosomes. This rendering was used to mask the VGLUT1 or Homer1 signal, and the Spots function was subsequently used to quantify the number of VGLUT1 puncta or Homer1 puncta entirely within the microglial surface or the surface of phagolysosome in individual microglia. Analysis was automated and the experimenter was blinded to genotype and experimental condition throughout. In some cases, data were normalized to the indicated control conditions to allow better comparisons between different experimental batches.

Quantification of c-Fos⁺ neurons

c-Fos⁺ neurons were quantified in ImageJ by first thresholding the NeuN channel to mask for individual neurons, thresholding the c-Fos channel, and analyzing the c-Fos⁺ neurons based on the NeuN mask image. Default thresholding was used for NeuN masking and MaxEntropy thresholding was used for c-Fos⁺ identification.

IL-33^{mCherry} quantification

In most cases, cells were scored as positive or negative. For intensity measurements, a 7.5-µm-thick Z-stack image was obtained using an LSM 800 confocal microscope (Zeiss), and the maximum intensity projection image was created. Mean fluorescent intensity was quantified in ImageJ by first thresholding the IL-33 channel to make a mask for an individual cell, then measuring the intensity of IL-33 channel of an individual cell in a grey scale, and averaging those values in a field of view.

Seizure behavior assays

Mice between P30 and P45 were used for seizure behavioral assays. PTZ (Sigma-Aldrich) and kainic acid (KA; Tocris) were dissolved in normal saline and freshly prepared. 50 mg/kg of PTZ or 16 mg/kg of KA was used. Each animal was placed in the center of a transparent cage immediately after IP injection of PTZ or KA, and the behavior was video recorded for 1 or 3 h, respectively. Video clips were analyzed to measure the latency to develop seizures, defined as generalized tonic–clonic seizure (GTC) with loss of balance or wild jumping (Lüttjohann et al., 2009), the number, and the duration of seizures. More than 10 s between two GTCs was considered as two separate events. After KA injection, 2/9 and 1/10 mice from control and IL33 cKO, respectively, which did not have a seizure, were excluded from the latency to seizure onset analysis, and 1/9 and 2/10 mice from control and IL33 cKO, respectively, which had a continuous prolonged seizure and died, were excluded from duration and the number of seizures analysis. Mice were sacrificed within 3 h after PTZ injection for the IHC experiment. All experiments were conducted in the same conditions between 10 AM and 4 PM, and the experimenter was blinded to genotype throughout data collection and analysis.

Implantation ECoG devices

Procedures were performed as previously described (Ritter-Makinson et al., 2019). Custom devices containing multiple screws were used to acquire ECoG signals in vivo (Mill-Max Manufacturing Corp). Animals were anesthetized with isoflurane (2–5%) and secured with ear bars in a stereotaxic frame while resting on top of a small heating pad to maintain body temperature. Small bur holes were drilled using a hand-held drill (Dremel) and were located above the prefrontal cortex (AP: +0.5 mm from Bregma) and somatosensory cortex (AP: −0.5 mm from Bregma, ML: +2.5 mm). The reference screw was placed above the cerebellum (AP: −1.0 mm from Lambda; ML: +1.0 mm). To implant ECoG devices, screws were placed into the bur holes and secured with dental cement. Topical lidocaine and antiseptic ointment were applied to the skin surrounding the implant. Animals were monitored for 1 wk as they recovered, prior to beginning recordings.

In vivo ECoG acquisition

Recordings were performed as previously described (Sorokin et al., 2017; Ritter-Makinson et al., 2019). ECoG signals were recorded at 24.41 kHz sampling rate using RZ5 and Synapse software (Tucker Davis Technologies). A video camera mounted on a flexible arm was used to continuously monitor the animals. Each recording trial consists of 60 min of baseline recording followed by 60 min of recording after a single dose 50 mg/kg PTZ intraperitoneal injection. ECoG signals from the prefrontal cortex and somatosensory cortex were referenced to the ECoG

screw electrode placed over the cerebellum. Analysis was performed using ClampFit (Molecular Devices) for spike and SWD analysis.

For spectral analysis, ECoG data were filtered with a second-order zero-phase Butterworth bandpass filter 0.5 and 300 Hz) and a stopband filter (60 Hz). Two-sided PSD estimates were obtained using Welch's method (window size, 10 s; 50% overlapping segments). Data are presented as relative PSD estimates, where PSD is normalized to the average total power of the recording (0.5–300 Hz range), within each subject. For spectral analyses, the relative PSD estimates are presented in the conventionally described frequency bands: Delta: 0.5–4 Hz; Theta: 4–8 Hz; Alpha: 8–12 Hz; Sigma: 12–15 Hz; Beta: 15–30 Hz; Gamma: 30–90 Hz; and High Gamma: 90–150 Hz. All recordings were performed from 9 AM to 6 PM.

For spike analysis, data were bandpass filtered at 1 and 100 Hz. A spike was defined as a signal that was >0.4 mV based on visual inspection of all recordings (mean standard deviation from mean spike amplitude [1 ± 3.6 µV] was 0.068 ± 0.015 mV).

For SWD analysis, data were bandpass-filtered at 1 and 60 Hz. SWDs were defined as at least five connected rhythmic 4–6 Hz spike-wave complexes (typically spanning at least 0.5 s) with amplitudes at least twofold higher than the background. All data were collected and analyzed blinded to genotype and condition.

Synapse quantification

Mice between P14 and P17 were used for synapse quantification after i.c.v. IL-33 injection. Mice between P28 and P35 were used for synapse quantification of *hGFAPCre;Il33*^{floxed} and *Cx3cr1-creER;Il1rl1*^{floxed} and their control experiments. Quantification was performed as previously described (Ippolito and Eroglu, 2010). Briefly, synapse colocalization for pre-and postsynaptic markers was quantified by determining colocalization of Homer1 and VGLUT1 or VGLUT2; Gephyrin and VGAT in optical sections of somatosensory thalamus and layer 4 sensory cortex. Images were collected using standardized imaging parameters throughout, and colocalization was analyzed using PunctaAnalyzer, an ImageJ plug-in developed by the Eroglu lab. Analysis parameters were constant throughout and blinded to genotype and condition. Image quality was checked by repeating analyses after 90° rotation of one channel to verify that colocalization was not due to random chance.

Statistical analysis

For statistical analysis, Graphpad Prism 8, 9, and R was used. Comparisons of two groups were performed with the two-tailed unpaired *t* test, the nonparametric Mann–Whitney test, or the Fisher's exact test, as needed. The difference between multiple groups was tested by one-way ANOVA followed by Tukey's test. Two-way ANOVA followed by Tukey's multiple comparison or Sidak's multiple comparison was used as needed when more than two comparisons were made. The level of significance was set at $P < 0.05$. RNA-sequencing and ATAC-seq data were analyzed in R as described in the Materials and methods section.

Online supplemental material

Fig. S1 shows the gating strategy for sequencing experiments, quality control of scRNA-seq, and other validation of microglial MARCO and TLR2 expression in response to IL-33 (data related to Fig. 1). Fig. S2 shows quality control of bulk RNA-, ATAC-, and ChIP-seq of microglia after IL-33 exposure (data related to Fig. 2). Fig. S3 shows validation of *Marco* and *Tlr2* deficient animals and the impact of TLR2 on microglial synapse refinement (data related to Fig. 3). Fig. S4 shows cellular sources of IL-33, the efficiency of IL-33 deletion using *hGFAP*^{cre}*:Il33*$^{fl/fl}$, and further analysis of synapse numbers and electrocorticography in IL-33 cKO (data related to Fig. 4). Fig. S5 shows further analysis of seizure phenotypes after conditional deletion of IL-33 (data related to Fig. 5). Table S1 includes scRNA-seq data showing differentially expressed genes per cluster. Table S2 includes a list of genes differentially expressed in microglia after IL-33 i.c.v. vs. vehicle, in bulk RNA-seq. Table S3 includes a list of ATAC-seq and H3K27ac ChIP-seq peaks differentially expressed in microglia after IL-33 i.c.v. vs. vehicle. Table S4 includes mEPSC and mIPSC amplitude and kinetics, and intrinsic electrical membrane properties of neurons in somatosensory thalamus of IL-33 cKO (*hGFAPCre+/−;Il33*$^{fl/fl}$) vs. littermate controls (*Il33*$^{fl/fl}$). Table S5 lists the reagents and resources used in this study.

Data availability

Marco KO mice were kindly provided by Dr. James Luyendyk under MTA AAGR2021-00156. All data needed to evaluate the conclusions in the paper are present in the paper or the Supplementary materials. Bulk RNA-, ATAC-, H3K27ac ChIP-seq, and scRNA-seq data of microglia post i.c.v. injection of IL-33 or vehicle are available from GEO with accession number GSE218428. ATAC-seq and ChIP-seq peaks can be visualized in the UCSC data browser (https://genome.ucsc.edu/s/jschlachetzki/IL33_Microglia_mm10).

Acknowledgments

We are grateful to members of the Molofsky Labs for helpful comments on the manuscript and to Irene Lew for help with animal husbandry. Thanks to Fumitaka Inoue for advice on ATAC-seq and Sven Heinz for advice on FOS ChIP-seq. Thanks to the UCSF Laboratory for Cell Analysis and Center for Advanced Technology for their technical contributions. Imaging was performed at the Gladstone Institutes' Histology & Light Microscopy Core.

A.V. Molofsky is supported by the Pew Charitable Trusts, the Brain and Behavior Research Foundation, National Institutes of Mental Health (R01MH119349, MH125000, and DP2MH116507), and the Burroughs Welcome Fund. This study was supported in part by the Helen Diller Family Comprehensive Cancer Center Laboratory for cell Analysis Shared Resource facility through a shared grant from National Institutes of Health (NIH; P30CA082103). J.T. Paz is supported by NIH and National Institute of Neurological Disorders and Stroke (NINDS) R01 NS096369-01, Department of Defense EP150038, National Science Foundation 1608236, and the Gladstone Institutes Animal Facility Grant RR18928. F.S. Cho is supported by NINDS NS111819. C.K. Glass is supported by NIH grant NS096170.

Authors contributions: Conceptualization: R.T. Han, I.D. Vainchtein, A.B. Molofsky, J.T. Paz, and A.V. Molofsky;

Methodology: R.T. Han, I.D. Vainchtein, F.S. Cho, and L.C. Dorman; Investigation: R.T. Han, I.D. Vainchtein, F.S. Cho, J.C.M. Schlachetzki, E. Ahn, D.K. Kim, J.J. Barron, and H. Nakao-Inoue; Writing—Original Draft: R.T. Han, I.D. Vainchtein, and A.V. Molofsky.; Writing—Review and Editing: all co-authors; Funding Acquisition: A.V. Molofsky; Resources: A.V. Molofsky and J.T. Paz; Supervision: A.V. Molofsky, C.K. Glass, and J.T. Paz.

Disclosures: The authors declare no competing interests exist.

Submitted: 6 April 2022
Revised: 21 September 2022
Accepted: 28 November 2022

References

Anders, S., P.T. Pyl, and W. Huber. 2015. HTSeq--a python framework to work with high-throughput sequencing data. *Bioinformatics*. 31:166–169. https://doi.org/10.1093/bioinformatics/btu638

Antoine, M.W., T. Langberg, P. Schnepel, and D.E. Feldman. 2019. Increased excitation-inhibition ratio stabilizes synapse and circuit excitability in four autism mouse models. *Neuron*. 101:648–661.e4. https://doi.org/10.1016/j.neuron.2018.12.026

Ayata, P., A. Badimon, H.J. Strasburger, M.K. Duff, S.E. Montgomery, Y.E. Loh, A. Ebert, A.A. Pimenova, B.R. Ramirez, A.T. Chan, et al. 2018. Epigenetic regulation of brain region-specific microglia clearance activity. *Nat. Neurosci.* 21:1049–1060. https://doi.org/10.1038/s41593-018-0192-3

Bennett, F.C., and A.V. Molofsky. 2019. The immune system and psychiatric disease: A basic science perspective. *Clin. Exp. Immunol.* 197:294–307. https://doi.org/10.1111/cei.13334

Bowdish, D.M.E., and S. Gordon. 2009. Conserved domains of the class A scavenger receptors: Evolution and function. *Immunol. Rev.* 227:19–31. https://doi.org/10.1111/j.1600-065X.2008.00728.x

Buenrostro, J.D., P.G. Giresi, L.C. Zaba, H.Y. Chang, and W.J. Greenleaf. 2013. Transposition of native chromatin for fast and sensitive epigenomic profiling of open chromatin, DNA-binding proteins and nucleosome position. *Nat. Methods*. 10:1213–1218. https://doi.org/10.1038/nmeth.2688

Butovsky, O., M.P. Jedrychowski, C.S. Moore, R. Cialic, A.J. Lanser, G. Gabriely, T. Koeglsperger, B. Dake, P.M. Wu, C.E. Doykan, et al. 2014. Identification of a unique TGF-β-dependent molecular and functional signature in microglia. *Nat. Neurosci.* 17:131–143. https://doi.org/10.1038/nn.3599

Creyghton, M.P., A.W. Cheng, G.G. Welstead, T. Kooistra, B.W. Carey, E.J. Steine, J. Hanna, M.A. Lodato, G.M. Frampton, P.A. Sharp, et al. 2010. Histone H3K27ac separates active from poised enhancers and predicts developmental state. *Proc. Natl. Acad. Sci. USA*. 107:21931–21936. https://doi.org/10.1073/pnas.1016071107

Crunelli, V., M.L. Lőrincz, C. McCafferty, R.C. Lambert, N. Leresche, G. Di Giovanni, and F. David. 2020. Clinical and experimental insight into pathophysiology, comorbidity and therapy of absence seizures. *Brain*. 143:2341–2368. https://doi.org/10.1093/brain/awaa072

DeNardo, L.A., C.D. Liu, W.E. Allen, E.L. Adams, D. Friedmann, L. Fu, C.J. Guenthner, M. Tessier-Lavigne, and L. Luo. 2019. Temporal evolution of cortical ensembles promoting remote memory retrieval. *Nat. Neurosci.* 22:460–469. https://doi.org/10.1038/s41593-018-0318-7

Dobin, A., C.A. Davis, F. Schlesinger, J. Drenkow, C. Zaleski, S. Jha, P. Batut, M. Chaisson, and T.R. Gingeras. 2013. STAR: Ultrafast universal RNA-seq aligner. *Bioinformatics*. 29:15–21. https://doi.org/10.1093/bioinformatics/bts635

Faust, T.E., G. Gunner, and D.P. Schafer. 2021. Mechanisms governing activity-dependent synaptic pruning in the developing mammalian CNS. *Nat. Rev. Neurosci.* 22:657–673. https://doi.org/10.1038/s41583-021-00507-y

Filipello, F., R. Morini, I. Corradini, V. Zerbi, A. Canzi, B. Michalski, M. Erreni, M. Markicevic, C. Starvaggi-Cucuzza, K. Otero, et al. 2018. The microglial innate immune receptor TREM2 is required for synapse elimination and normal brain connectivity. *Immunity*. 48:979–991.e8. https://doi.org/10.1016/j.immuni.2018.04.016

Finak, G., A. McDavid, M. Yajima, J. Deng, V. Gersuk, A.K. Shalek, C.K. Slichter, H.W. Miller, M.J. McElrath, M. Prlic, et al. 2015. MAST: A flexible statistical framework for assessing transcriptional changes and characterizing heterogeneity in single-cell RNA sequencing data. *Genome Biol.* 16:278. https://doi.org/10.1186/s13059-015-0844-5

Fourgeaud, L., P.G. Través, Y. Tufail, H. Leal-Bailey, E.D. Lew, P.G. Burrola, P. Callaway, A. Zagórska, C.V. Rothlin, A. Nimmerjahn, and G. Lemke. 2016. TAM receptors regulate multiple features of microglial physiology. *Nature*. 532:240–244. https://doi.org/10.1038/nature17630

Frost, J.L., and D.P. Schafer. 2016. Microglia: Architects of the developing nervous system. *Trends Cell Biol.* 26:587–597. https://doi.org/10.1016/j.tcb.2016.02.006

Galatro, T.F., I.D. Vainchtein, N. Brouwer, E.W.G.M. Boddeke, and B.J.L. Eggen. 2017. Isolation of microglia and immune infiltrates from mouse and primate central nervous system. *Methods Mol. Biol.* 1559:333–342. https://doi.org/10.1007/978-1-4939-6786-5_23

Gazon, H., B. Barbeau, J.M. Mesnard, and J.M. Peloponese Jr. 2018. Hijacking of the AP-1 signaling pathway during development of ATL. *Front. Microbiol.* 8:2686. https://doi.org/10.3389/fmicb.2017.02686

Golshani, P., R.A. Warren, and E.G. Jones. 1998. Progression of change in NMDA, non-NMDA, and metabotropic glutamate receptor function at the developing corticothalamic synapse. *J. Neurophysiol.* 80:143–154. https://doi.org/10.1152/jn.1998.80.1.143

Gosselin, D., V.M. Link, C.E. Romanoski, G.J. Fonseca, D.Z. Eichenfield, N.J. Spann, J.D. Stender, H.B. Chun, H. Garner, F. Geissmann, and C.K. Glass. 2014. Environment drives selection and function of enhancers controlling tissue-specific macrophage identities. *Cell*. 159:1327–1340. https://doi.org/10.1016/j.cell.2014.11.023

Gosselin, D., D. Skola, N.G. Coufal, I.R. Holtman, J.C.M. Schlachetzki, E. Sajti, B.N. Jaeger, C. O'Connor, C. Fitzpatrick, M.P. Pasillas, et al. 2017. An environment-dependent transcriptional network specifies human microglia identity. *Science*. 356:1248–1259. https://doi.org/10.1126/science.aal3222

Hafemeister, C. and R. Satija. 2019. Normalization and variance stabilization of single-cell RNA-seq data using regularized negative binomial regression. *Genome Biol.* 20:296. https://doi.org/10.1186/s13059-019-1874-1

Hao, Y., S. Hao, E. Andersen-nissen, W.M.M. Iii, S. Zheng, M.J. Lee, A.J. Wilk, C. Darby, M. Zagar, P. Hoffman, et al. 2020. Integrated analysis of multimodal single-cell data Yuhan. (Preprint posted October 12, 2020). *bioRxiv*. https://doi.org/10.1101/2020.10.12.335331

He, D., H. Xu, H. Zhang, R. Tang, Y. Lan, R. Xing, S. Li, E. Christian, Y. Hou, P. Lorello, et al. 2022. Disruption of the IL-33-ST2-AKT signaling axis impairs neurodevelopment by inhibiting microglial metabolic adaptation and phagocytic function. *Immunity*. 55:159–173.e9. https://doi.org/10.1016/j.immuni.2021.12.001

Heinz, S., C. Benner, N. Spann, E. Bertolino, Y.C. Lin, P. Laslo, J.X. Cheng, C. Murre, H. Singh, and C.K. Glass. 2010. Simple combinations of lineage-determining transcription factors prime cis-regulatory elements required for macrophage and B cell identities. *Mol. Cell*. 38:576–589. https://doi.org/10.1016/j.molcel.2010.05.004

Hoffman, G.E., and E.E. Schadt. 2016. variancePartition: Interpreting drivers of variation in complex gene expression studies. *BMC Bioinformatics*. 17:483. https://doi.org/10.1186/s12859-016-1323-z

Holtman, I.R., D. Skola, and C.K. Glass. 2017. Transcriptional control of microglia phenotypes in health and disease. *J. Clin. Invest.* 127:3220–3229. https://doi.org/10.1172/JCI90604

Hrvatin, S., D.R. Hochbaum, M.A. Nagy, M. Cicconet, K. Robertson, L. Cheadle, R. Zilionis, A. Ratner, R. Borges-Monroy, A.M. Klein, et al. 2018. Single-cell analysis of experience-dependent transcriptomic states in the mouse visual cortex. *Nat. Neurosci.* 21:120–129. https://doi.org/10.1038/s41593-017-0029-5

Huguenard, J.R., and D.A. McCormick. 2007. Thalamic synchrony and dynamic regulation of global forebrain oscillations. *Trends Neurosci.* 30:350–356. https://doi.org/10.1016/j.tins.2007.05.007

Ippolito, D.M., and C. Eroglu. 2010. Quantifying synapses: An immunocytochemistry-based assay to quantify synapse number. *J. Vis. Exp.*:12270. https://doi.org/10.3791/2270

Jung, S., J. Aliberti, P. Graemmel, M.J. Sunshine, G.W. Kreutzberg, A. Sher, and D.R. Littman. 2000. Analysis of fractalkine receptor CX_3CR1 function by targeted deletion and green fluorescent protein reporter gene insertion. *Mol. Cell. Biol.* 20:4106–4114. https://doi.org/10.1128/mcb.20.11.4106-4114.2000

Kent, W.J., C.W. Sugnet, T.S. Furey, K.M. Roskin, T.H. Pringle, A.M. Zahler, and D. Haussler. 2002. The human genome browser at UCSC. *Genome Res.* 12:996–1006. https://doi.org/10.1101/gr.229102

Korsunsky, I., N. Millard, J. Fan, K. Slowikowski, F. Zhang, K. Wei, Y. Baglaenko, M. Brenner, P.R. Loh, and S. Raychaudhuri. 2019. Fast, sensitive and accurate integration of single-cell data with Harmony. *Nat. Methods*. 16:1289–1296. https://doi.org/10.1038/s41592-019-0619-0

Langmead, B., and S.L. Salzberg. 2012. Fast gapped-read alignment with Bowtie 2. *Nat. Methods*. 9:357–359. https://doi.org/10.1038/nmeth.1923

Lau, S.F., C. Chen, W.Y. Fu, J.Y. Qu, T.H. Cheung, A.K.Y. Fu, and N.Y. Ip. 2020. IL-33-PU.1 transcriptome reprogramming drives functional state transition and clearance activity of microglia in Alzheimer's disease. *Cell Rep.* 31:107530. https://doi.org/10.1016/j.celrep.2020.107530

Lavin, Y., D. Winter, R. Blecher-Gonen, E. David, H. Keren-Shaul, M. Merad, S. Jung, and I. Amit. 2014. Tissue-resident macrophage enhancer landscapes are shaped by the local microenvironment. *Cell*. 159: 1312–1326. https://doi.org/10.1016/j.cell.2014.11.018

Love, M.I., W. Huber, and S. Anders. 2014. Moderated estimation of fold change and dispersion for RNA-seq data with DESeq2. *Genome Biol.* 15: 550. https://doi.org/10.1186/s13059-014-0550-8

Lüttjohann, A., P.F. Fabene, and G. van Luijtelaar. 2009. A revised Racine's scale for PTZ-induced seizures in rats. *Physiol. Behav.* 98:579–586. https://doi.org/10.1016/j.physbeh.2009.09.005

Lüttjohann, A., and G. van Luijtelaar. 2015. Dynamics of networks during absence seizure's on- and offset in rodents and man. *Front. Physiol.* 6:16. https://doi.org/10.3389/fphys.2015.00016

McKinsey, G.L., C.O. Lizama, A.E. Keown-Lang, A. Niu, N. Santander, A. Larpthaveesarp, E. Chee, F.F. Gonzalez, and T.D. Arnold. 2020. A new genetic strategy for targeting microglia in development and disease. *Elife*. 9:1–34. https://doi.org/10.7554/eLife.54590

Medzhitov, R., and C. Janeway Jr. 2000. The Toll receptor family and microbial recognition. *Trends Microbiol.* 8:452–456. https://doi.org/10.1016/S0966-842X(00)01845-X

Midorikawa, M., and M. Miyata. 2021. Distinct functional developments of surviving and eliminated presynaptic terminals. *Proc. Natl. Acad. Sci. USA*. 118:e2022423118. https://doi.org/10.1073/pnas.2022423118

Molofsky, A.V., K.W. Kelley, H.H. Tsai, S.A. Redmond, S.M. Chang, L. Madireddy, J.R. Chan, S.E. Baranzini, E.M. Ullian, and D.H. Rowitch. 2014. Astrocyte-encoded positional cues maintain sensorimotor circuit integrity. *Nature*. 509:189–194. https://doi.org/10.1038/nature13161

Mosser, C.A., S. Baptista, I. Arnoux, and E. Audinat. 2017. Microglia in CNS development: Shaping the brain for the future. *Prog. Neurobiol.* 149-150: 1–20. https://doi.org/10.1016/j.pneurobio.2017.01.002

Nguyen, P.T., L.C. Dorman, S. Pan, I.D. Vainchtein, R.T. Han, H. Nakao-Inoue, S.E. Taloma, J.J. Barron, A.B. Molofsky, M.A. Kheirbek, and A.V. Molofsky. 2020. Microglial remodeling of the extracellular matrix promotes synapse plasticity. *Cell*. 182:388–403.e15. https://doi.org/10.1016/j.cell.2020.05.050

Nott, A., I.R. Holtman, N.G. Coufal, J.C.M. Schlachetzki, M. Yu, R. Hu, C.Z. Han, M. Pena, J. Xiao, Y. Wu, et al. 2019. Brain cell type-specific enhancer-promoter interactome maps and disease-risk association. *Science*. 366:1134–1139. https://doi.org/10.1126/science.aay0793

Paz, J.T., T.J. Davidson, E.S. Frechette, B. Delord, I. Parada, K. Peng, K. Deisseroth, and J.R. Huguenard. 2013. Closed-loop optogenetic control of thalamus as a tool for interrupting seizures after cortical injury. *Nat. Neurosci.* 16:64–70. https://doi.org/10.1038/nn.3269

Pinheiro da Silva, F., M. Aloulou, D. Skurnik, M. Benhamou, A. Andremont, I.T. Velasco, M. Chiamolera, J.S. Verbeek, P. Launay, and R.C. Monteiro. 2007. CD16 promotes *Escherichia coli* sepsis through an FcR γ inhibitory pathway that prevents phagocytosis and facilitates inflammation. *Nat. Med.* 13:1368–1374. https://doi.org/10.1038/nm1665

Ritter-Makinson, S., A. Clemente-Perez, B. Higashikubo, F.S. Cho, S.S. Holden, E. Bennett, A. Chkhaidze, O.H.J. Eelkman Rooda, M.C. Cornet, F.E. Hoebeek, et al. 2019. Augmented reticular thalamic bursting and seizures in scn1a-dravet syndrome. *Cell Rep.* 26:54–64.e6. https://doi.org/10.1016/j.celrep.2018.12.018

Rowley, J.W., A.J. Oler, N.D.O. Tolley, B.N. Hunter, E.N. Low, D.A. Nix, C.C. Yost, G.A. Zimmerman, and A.S. Weyrich. 2011. Genome-wide RNA-seq analysis of human and mouse platelet transcriptomes. *Blood*. 118: e101–e111. https://doi.org/10.1182/blood-2011-03-339705

Ruland, J. 2011. Return to homeostasis: Downregulation of NF-κB responses. *Nat. Immunol.* 12:709–714. https://doi.org/10.1038/ni.2055

Satija, R., J.A. Farrell, D. Gennert, A.F. Schier, and A. Regev. 2015. Spatial reconstruction of single-cell gene expression data. *Nat. Biotechnol.* 33: 495–502. https://doi.org/10.1038/nbt.3192

Schaefer, L., A. Babelova, E. Kiss, H.J. Hausser, M. Baliova, M. Krzyzankova, G. Marsche, M.F. Young, D. Mihalik, M. Götte, et al. 2005. The matrix component biglycan is proinflammatory and signals through Toll-like receptors 4 and 2 in macrophages. *J. Clin. Invest.* 115:2223–2233. https://doi.org/10.1172/JCI23755

Shirotani, K., Y. Hori, R. Yoshizaki, E. Higuchi, M. Colonna, T. Saito, S. Hashimoto, T. Saito, T.C. Saido, and N. Iwata. 2019. Aminophospholipids are signal-transducing TREM2 ligands on apoptotic cells. *Sci. Rep.* 9: 7508. https://doi.org/10.1038/s41598-019-43535-6

Sohal, V.S., and J.L.R. Rubenstein. 2019. Excitation-inhibition balance as a framework for investigating mechanisms in neuropsychiatric disorders. *Mol. Psychiatry*. 24:1248–1257. https://doi.org/10.1038/s41380-019-0426-0

Sorokin, J.M., T.J. Davidson, E. Frechette, A.M. Abramian, K. Deisseroth, J.R. Huguenard, and J.T. Paz. 2017. Bidirectional control of generalized epilepsy networks via rapid real-time switching of firing mode. *Neuron*. 93:194–210. https://doi.org/10.1016/j.neuron.2016.11.026

Takeuchi, Y., H. Asano, Y. Katayama, Y. Muragaki, K. Imoto, and M. Miyata. 2014. Large-scale somatotopic refinement via functional synapse elimination in the sensory thalamus of developing mice. *J. Neurosci.* 34: 1258–1270. https://doi.org/10.1523/JNEUROSCI.3865-13.2014

Texari, L., N.J. Spann, T.D. Troutman, M. Sakai, J.S. Seidman, and S. Heinz. 2021. An optimized protocol for rapid, sensitive and robust on-bead ChIP-seq from primary cells. *STAR Protoc.* 2:100358. https://doi.org/10.1016/j.xpro.2021.100358

Thompson, M.R., D. Xu, and B.R.G. Williams. 2009. ATF3 transcription factor and its emerging roles in immunity and cancer. *J. Mol. Med.* 87: 1053–1060. https://doi.org/10.1007/s00109-009-0520-x

Troutman, T.D., E. Kofman, and C.K. Glass. 2021. Exploiting dynamic enhancer landscapes to decode macrophage and microglia phenotypes in health and disease. *Mol. Cell*. 81:3888–3903. https://doi.org/10.1016/j.molcel.2021.08.004

Vainchtein, I.D., G. Chin, F.S. Cho, K.W. Kelley, J.G. Miller, E.C. Chien, S.A. Liddelow, P.T. Nguyen, H. Nakao-Inoue, L.C. Dorman, et al. 2018. Astrocyte-derived interleukin-33 promotes microglial synapse engulfment and neural circuit development. *Science*. 1273:1269–1273. https://doi.org/10.1126/science.aal3589

van der Laan, L.J., E.A. Döpp, R. Haworth, T. Pikkarainen, M. Kangas, O. Elomaa, C.D. Dijkstra, S. Gordon, K. Tryggvason, and G. Kraal. 1999. Regulation and functional involvement of macrophage scavenger receptor MARCO in clearance of bacteria in vivo. *J. Immunol.* 162:939–947

Vezzani, A., B. Lang, and E. Aronica. 2015. Immunity and inflammation in epilepsy. *Cold Spring Harb. Perspect. Med.* 6:a022699. https://doi.org/10.1101/cshperspect.a022699

Wilkinson, K., and J. El Khoury. 2012. Microglial scavenger receptors and their roles in the pathogenesis of Alzheimer's disease. *Int. J. Alzheimers Dis.* 2012:489456. https://doi.org/10.1155/2012/489456

Xu, J., A. Flaczyk, L.M. Neal, Z. Fa, A.J. Eastman, A.N. Malachowski, D. Cheng, B.B. Moore, J.L. Curtis, J.J. Osterholzer, and M.A. Olszewski. 2017. Scavenger receptor MARCO orchestrates early defenses and contributes to fungal containment during cryptococcal infection. *J. Immunol.* 198:3548–3557. https://doi.org/10.4049/jimmunol.1700057

Yona, S., K.W. Kim, Y. Wolf, A. Mildner, D. Varol, M. Breker, D. Strauss-Ayali, S. Viukov, M. Guilliams, A. Misharin, et al. 2013. Fate mapping reveals origins and dynamics of monocytes and tissue macrophages under homeostasis. *Immunity*. 38:79–91. https://doi.org/10.1016/j.immuni.2012.12.001

Yoshida, M., T. Satoh, K.C. Nakamura, T. Kaneko, and Y. Hata. 2009. Cortical activity regulates corticothalamic synapses in dorsal lateral geniculate nucleus of rats. *Neurosci. Res.* 64:118–127. https://doi.org/10.1016/j.neures.2009.02.002

Zaret, K.S. 2020. Pioneer transcription factors initiating gene network changes. *Annu. Rev. Genet.* 54:367–385. https://doi.org/10.1146/annurev-genet-030220-015007

Zhou, Y., B. Zhou, L. Pache, M. Chang, A.H. Khodabakhshi, O. Tanaseichuk, C. Benner, and S.K. Chanda. 2019. Metascape provides a biologist-oriented resource for the analysis of systems-level datasets. *Nat. Commun.* 10: 1523. https://doi.org/10.1038/s41467-019-09234-6

Zhuo, L., M. Theis, I. Alvarez-Maya, M. Brenner, K. Willecke, and A. Messing. 2001. hGFAP-cre transgenic mice for manipulation of glial and neuronal function in vivo. *Genesis*. 31:85–94. https://doi.org/10.1002/gene.10008

Zolnik, T.A., and B.W. Connors. 2016. Electrical synapses and the development of inhibitory circuits in the thalamus. *J. Physiol.* 10:2579–2592. https://doi.org/10.1113/JP271880

Supplemental material

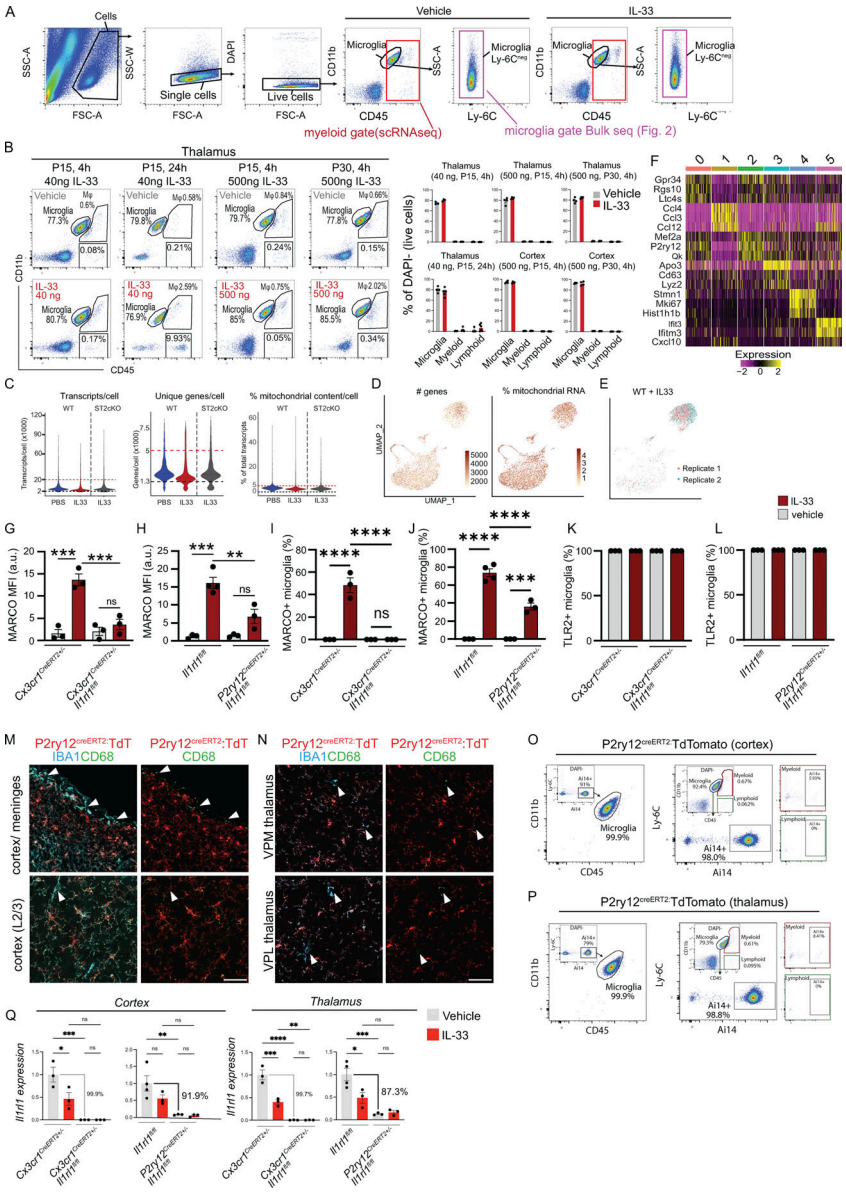

Figure S1. **Quality control of single-cell sequencing of microglial response to IL-33. (A)** Gating strategy for isolation by FACS of all CD45$^+$ (red) for scRNA-seq in Fig. 1, or microglia only (CD11b$^+$, CD45^{low}, Ly-6C$^-$, violet) for bulk RNA-/ATAC-/ChIP-seq (Fig. 2). **(B)** Gating strategy showing microglia (CD45^{low}CD11b$^+$), myeloid (CD45^{high}CD11b$^+$), and lymphoid cells (CD45$^+$CD11b$^-$) after vehicle or IL-33, gated on CD11b and CD45. Representative plots from thalamus, quantifications include thalamus and cortex. Dots = mice. **(C)** Violin plots of scRNA-seq data showing transcripts/cell, unique genes/cell, and percentage mitochondrial content/cell for each sample. Cut-off boundaries are marked (upper: red line; bottom: black line). **(D)** Feature plots for the number of genes and percentage mitochondrial RNA for all samples combined from scRNA-seq data. Each dot represents a cell. **(E)** Feature plot showing correlation between two replicates used for WT + IL-33 scRNA-seq sample. **(F)** Heatmap for the top three genes in each cluster from scRNA-seq data. **(G and H)** Mean fluorescence intensity for MARCO protein in cortex from Cx3cr1^{creERT2} (G) and P2ry12-^{creERT2} (H) mice. Dots = individual mice. Two-way ANOVA with Tukey's post hoc comparison (genotype and treatment). **(I and J)** Percentage of microglia expressing MARCO protein in thalamus from Cx3cr1^{creERT2} (I) and P2ry12-^{creERT2} (J) mice. Dots = individual mice. Two-way ANOVA with Tukey's post hoc comparison (genotype and treatment). **(K and L)** Percentage of microglia expressing TLR2 protein in thalamus from Cx3cr1^{creERT2} (K) and P2ry12-^{creERT2} (L) mice. Dots = individual mice. Two-way ANOVA with Tukey's post hoc comparison (genotype and treatment). **(M and N)** Representative images for P2ry12^{creERT2} crossed to a R26R-TdTomato (TdT) reporter (*Ai14*). **(M)** Top row shows cortex with overlying meninges. Arrowheads indicate meningeal macrophages that are CD68$^+$IBA1$^+$TdT$^-$. Bottom row shows L2/3 cortex. Arrowhead indicates perivascular macrophage that is CD68$^+$IBA1$^+$TdT$^-$. **(N)** Ventral posteromedial (VPM; top) and ventral posterolateral (VPL; bottom) nuclei of thalamus. Arrowhead indicates perivascular macrophage that is CD68$^+$IBA1$^+$TdT$^-$. Scale bar = 50 µm. **(O and P)** Representative flow plots of cortex (O) and thalamus (P) showing P2ry12^{creERT2} driven Ai14 (TdTomato) expression at P15. Two gating strategies shown: Left panel shows that of Ai14$^+$ cells, 99.9% fell within the CD45/CD11b microglial gate. Right panels pre-gate on microglia, myeloid, and lymphoid cells based on CD11b and CD45 followed by Ly-6C and Ai14, to show the percentage of each population with detectable TdT. **(Q)** qRT-PCR of *Il1rl1* expression in cortical and thalamic microglia comparing Cx3cr1^{creERT2} and P2ry12^{creERT2} mice. Values normalized to housekeeper (Hmbs) and then control + vehicle (PBS) condition. In Cx3cr1^{creERT2} the control = Cx3cr1$^{creERT2+/-}$ + vehicle (PBS). In P2ry12^{creERT2} the control = Il1rl1$^{fl/fl}$ + vehicle (PBS). Each dot represents a mouse. Two-way ANOVA followed by Tukey's post hoc comparison (genotype and treatment). Data points represent the average of three technical repeats for Cx3cr1^{creERT} and two technical repeats for P2ry12^{creERT}. Data represented as mean ± SEM for bar graphs. *P < 0.05, **P < 0.01, ***P < 0.001, ****P < 0.0001.

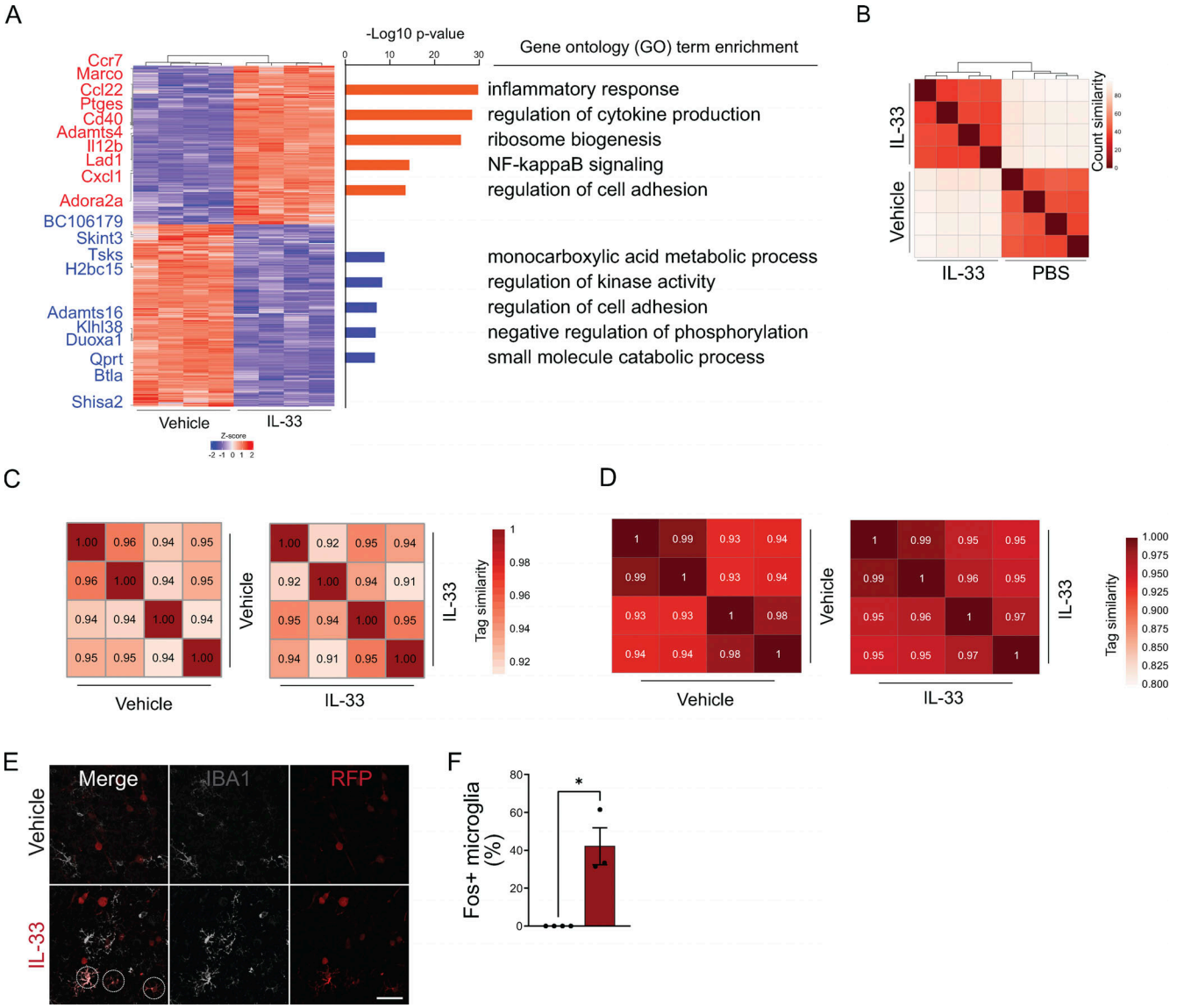

Figure S2. **Quality control for bulk transcriptomic and epigenomic profiling of microglia after IL-33 exposure. (A)** Heatmap of differentially expressed genes (DEG) in cortical microglia 4 h after vehicle (PBS) or 500 ng of IL-33 treatment (P_{adj} < 0.01). Left: Top 10 up- (red) and downregulated (blue) genes indicated. Right: Top GO categories associated with DEG (P_{adj} < 0.01, fold-change > 2). **(B)** Heatmap of sample-to-sample Pearson correlation of bulk RNA-seq replicates. **(C)** Heatmaps of sample-to-sample correlation for ATAC-seq replicates. Values indicate Pearson correlation. **(D)** Heatmaps of sample-to-sample correlation for H2K27ac ChIP-seq replicates. Values indicate Pearson correlation. **(E)** Low magnification representative images of staining for Fos-TRAP (TdT^+) after vehicle or IL-33 injection. Scale bar = 40 µm. **(F)** Percentage of Fos^+ microglia in the cortex after vehicle or IL-33 injection. Dots = mice. Two-tailed unpaired *t* test. Data represented as mean ± SEM for F. *P < 0.05.

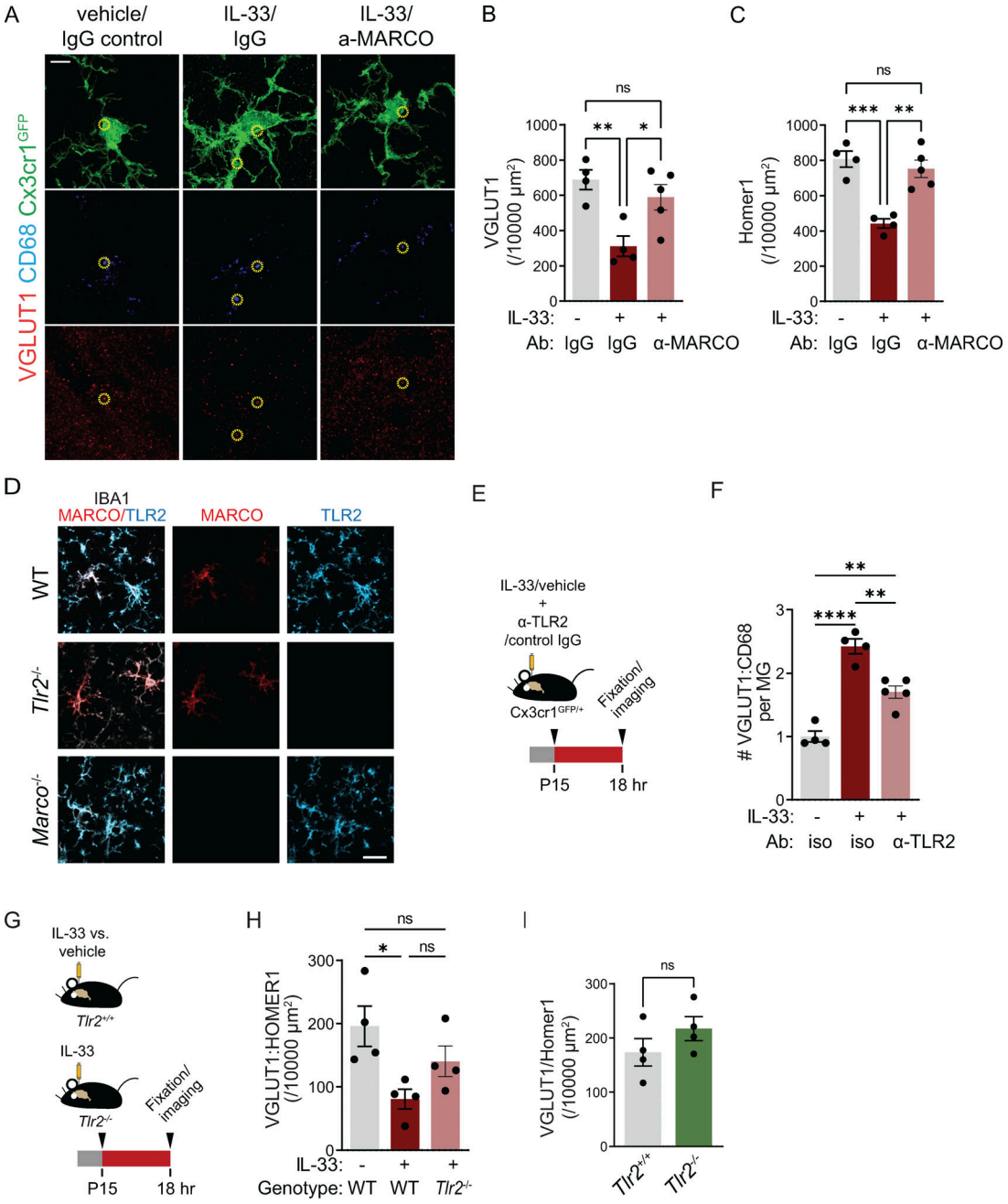

Figure S3. **Validation of MARCO and TLR2 deficient animals and impact of TLR2 on synapses. (A)** Representative images separated into individual channels for presynaptic protein (VGLUT1), phagolysosome (CD68), and *Cx3cr1*^{GFP} microglia (GFP) from a Z-stack maximum projection in the somatosensory thalamus for the indicated conditions. Vehicle = PBS. Yellow circles indicate representative colocalized VGLUT1 inside lysosomes (not all colocalized puncta are indicated.) Scale bar = 5 µm. **(B and C)** Same data as in Fig. 3 E, presented without colocalization, demonstrating changes in pre- (B) and post- (C) synaptic protein puncta of corticothalamic synapses in somatosensory thalamus 18 h after vehicle or IL-33 injection in the presence of MARCO blocking antibody or isotype control (n = 4 mice for vehicle + isotype control, n = 4 mice for IL-33 + isotype control, and n = 5 mice for IL-33 + α-MARCO). **(D)** Representative images of MARCO and TLR2 immunostaining in wild-type (top), *Tlr2*-deficient (middle) or *Marco*-deficient (bottom) animals to illustrate the specificity of antibody and lack of protein in *Marco*$^{-/-}$ and *Tlr2*$^{-/-}$ animals. Experiments were done 18 h after 40 ng of IL-33 i.c.v. injection at P17. Scale bar = 20 µm. **(E)** Schematic of i.c.v. injection of IL-33 and TLR2 blocking antibody in *Cx3cr1*^{GFP} reporter animals. **(F)** Quantification of VGLUT1 within CD68^{+} phagolysosomes within individual microglia 18 h after vehicle or IL-33 injection in the presence of TLR2 blocking antibody or isotype control (values normalized to vehicle + isotype control condition; n = 4 mice for vehicle + isotype control and IL-33 + isotype control, and n = 5 mice for IL33 + TLR2 blocking antibody). Age P15–P16. Data points represent the average of three technical repeats. **(G)** Schematic of i.c.v. injection of IL-33 in *Tlr2*$^{+/+}$ *or Tlr2*$^{-/-}$ animals. **(H)** Quantification of corticothalamic synapses in somatosensory thalamus 18 h after vehicle or IL-33 injection into *Tlr2*$^{+/+}$ and *Tlr2*$^{-/-}$ mice (n = 4 mice/condition). Age P15–P16. Data points represent the average of three technical repeats. **(I)** Quantification of excitatory synapses in ventrobasal thalamus of *Tlr2*$^{+/+}$ and *Tlr2*$^{-/-}$ mice. n = 4 mice/condition. Age P28–P30. Data points represent the average of two technical repeats. Dots = independent mice. Data represented as mean ± SEM for bar graphs. One-way ANOVA followed by post hoc Tukey's comparison was used for all analysis except I. Two-tailed unpaired t test was used for I. *P < 0.05, **P < 0.01, ***P < 0.001, ****P < 0.0001.

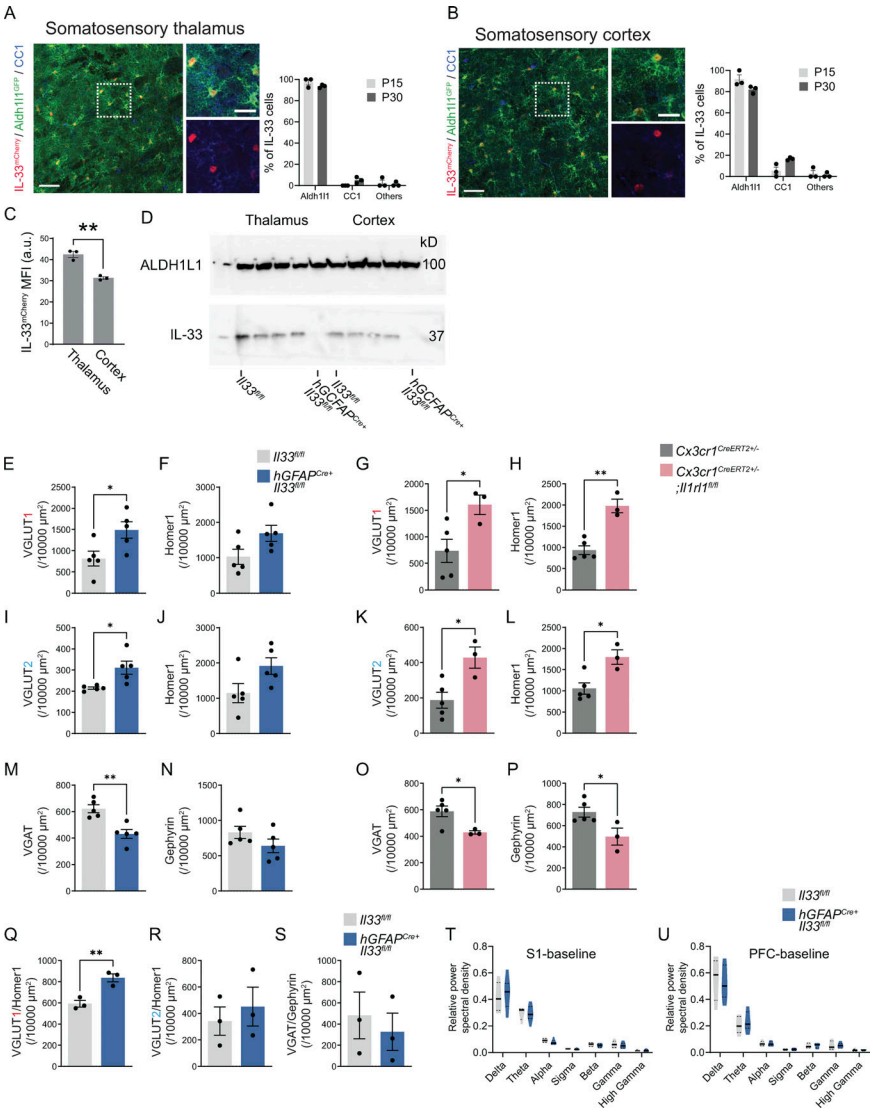

Figure S4. **Cellular sources of IL-33, efficiency of IL-33 depletion using *hGFAPcre:Il33*$^{fl/fl}$, and further analysis of cortical synapse numbers and electrocorticography in IL-33 cKO. (A)** Representative image and quantification of percent IL-33$^{mCherry+}$ cells in the somatosensory thalamus of *Il33*^{mCherry}; *Aldh1l1*^{GFP} mice stained with CC1 (oligodendrocytes) at P15 and P30. GFP expression marks astrocytes. Scale bars = 50 µm (left) and 20 µm (inset). **(B)** Representative image and quantification of percent IL-33$^{mCherry+}$ cells in the somatosensory cortex of *Il33*^{mCherry};*Aldh1l1*^{GFP} mice stained with CC1 (oligodendrocytes) at P15 and P30. Scale bars = 50 µm (left) and 20 µm (inset). **(C)** Comparison of mean fluorescent intensity (MFI) of IL-33^{mCherry} in the thalamus and the cortex at P15. **(D)** Western blot from cortex and thalamus of *hGFAP*$^{Cre+}$:*Il33*$^{fl/fl}$ animals and *Il33*$^{fl/fl}$ controls at P35. ALDH1L1 used as a loading control. **(E and F)** The same data as in Fig. 4 B, presented separately for pre- and postsynaptic excitatory synaptic proteins. Quantification of pre- (E) and post- (F) synaptic terminal of corticothalamic excitatory synapses in ventrobasal thalamus of *hGFAP*$^{Cre+}$;*Il33*$^{fl/fl}$ vs. *Il33*$^{fl/fl}$ control. *n* = 5 mice/genotype. Two-tailed unpaired *t* test. **(G and H)** The same data as in Fig. 4 C, presented separately for pre- and postsynaptic excitatory synaptic proteins. Quantification of pre- (G) and post- (H) synaptic terminal of corticothalamic excitatory synapses in ventrobasal thalamus of *Cx3cr1*$^{CreERT2+/-}$;*Il1rl1*$^{fl/fl}$) vs. *Cx3cr1*$^{CreERT2+/-}$. *Cx3cr1*$^{CreERT2+/-}$;*Il1rl1*$^{fl/fl}$: *n* = 3 mice. *Cx3cr1*$^{CreERT2+/-}$: *n* = 5 mice. Two-tailed unpaired *t* test. **(I and J)** The same data as in Fig. 4 E, presented separately for pre- and postsynaptic excitatory synaptic proteins. Quantification of pre- (I) and post- (J) synaptic terminal of brainstem afferent excitatory synapses in ventrobasal thalamus of *hGFAP*$^{Cre+}$;*Il33*$^{fl/fl}$ vs. *Il33*$^{fl/fl}$ control. *n* = 5 mice/genotype. Two-tailed unpaired *t* test. **(K and L)** The same data as in Fig. 4 F, presented separately for pre- and postsynaptic excitatory synaptic proteins. Quantification of pre- (K) and post- (L) synaptic terminal of brainstem afferent excitatory synapses in ventrobasal thalamus of *Cx3cr1*$^{CreERT2+/-}$;*Il1rl1*$^{fl/fl}$) vs. *Cx3cr1*$^{CreERT2+/-}$. *Cx3cr1*$^{CreERT2+/-}$;*Il1rl1*$^{fl/fl}$: *n* = 3 mice. *Cx3cr1*$^{CreERT2+/-}$: *n* = 5 mice. Two-tailed unpaired *t* test. **(M and N)** The same data as in Fig. 4 H, presented separately for pre- and postsynaptic excitatory synaptic proteins. Quantification of pre- (M) and post- (N) synaptic terminal of thalamic inhibitory synapses in *hGFAP*$^{Cre+}$;*Il33*$^{fl/fl}$ vs. *Il33*$^{fl/fl}$ control. *n* = 5 mice/genotype. Two-tailed unpaired *t* test. **(O and P)** The same data as in Fig. 4 I, presented separately for pre- and postsynaptic excitatory synaptic proteins. Quantification of pre- (O) and post- (P) synaptic terminal of thalamic inhibitory synapse in *Cx3cr1*$^{CreERT2+/-}$;*Il1rl1fl/f*) vs. *Cx3cr1*$^{CreERT2+/-}$. *Cx3cr1*$^{CreERT2+/-}$;*Il1rl1fl/fl*: *n* = 3 mice. *Cx3cr1*$^{CreERT2+/-}$: *n* = 5 mice. Two-tailed unpaired *t* test. **(Q–S)** Quantification of synapses in somatosensory cortex in *Il33*$^{fl/lfl}$ and *hGFAP*$^{Cre+}$:*Il33*$^{fl/fl}$ animals, including excitatory intracortical (Q), excitatory thalamocortical (R), and inhibitory (S) synapses. *n* = 3 *Il33*$^{fl/lfl}$ and *n* = 3 *hGFAP*$^{Cre+}$:*Il33*$^{fl/fl}$ mice in Q–S. Two-tailed unpaired *t* test. **(T and U)** Relative power of ECoG frequency bands from baseline recording in somatosensory (S1, T) and PFC (U) cortices. (*n* = 10 hGFAP^{Cre+}: IL33$^{fl/fl}$ mice and 8 littermate IL33$^{fl/fl}$ controls; two-way ANOVA followed by Sidak's multiple comparison). In all bar graphs, dots represent independent mice. Delta: 0.5–4 Hz; Theta: 4–8 Hz; Alpha: 8–12 Hz; Sigma: 12–15 Hz; Beta: 15–30 Hz; Gamma: 30–90 Hz; High Gamma: 90–150 Hz. Data are shown as mean ± SEM for bar graphs and as median ± interquartile range for violin plots. Mice from P28–P35 were used for E–S. *P < 0.05, **P < 0.01. Source data are available for this figure: SourceData FS4.

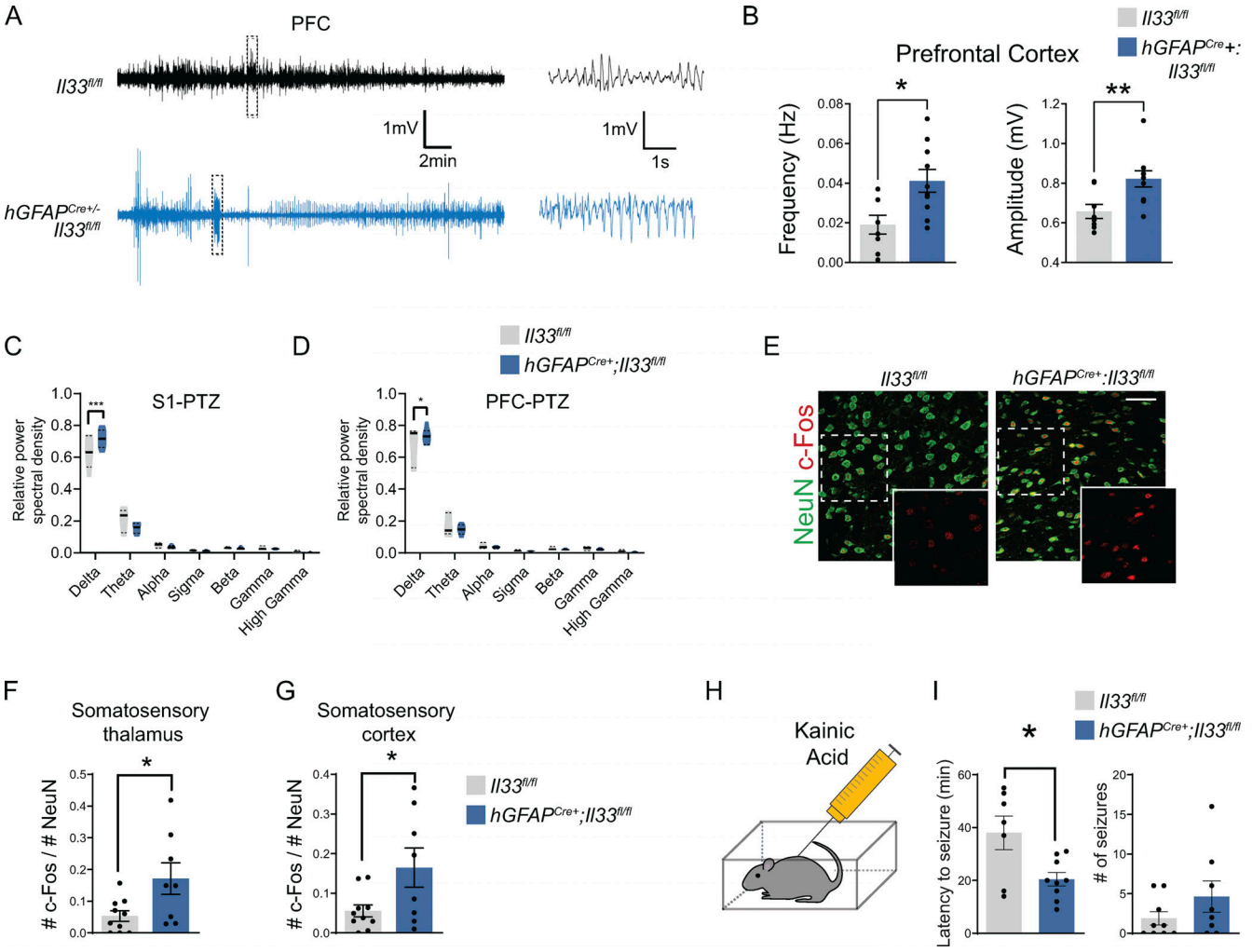

Figure S5. **Additional characterization of seizure phenotypes after conditional deletion of IL-33. (A and B)** Representative traces and quantification of total spike frequency (left) and average amplitude (right) of detected spike events from prefrontal cortex during 1-h recording session. *n* = 10 *hGFAP*$^{Cre+}$;*Il33*$^{fl/fl}$ mice and *n* = 8 *Il33*$^{fl/fl}$ mice (two-tailed unpaired *t* test). Each dot represents a mouse. Mice were P35–P45. **(C and D)** Relative power of ECoG frequency bands from somatosensory (C) and prefrontal (D) cortices after PTZ administration (*n* = 10 IL-33 hGFAP^{Cre+}: IL33$^{fl/fl}$ mice and 8 littermate IL33$^{fl/fl}$ controls; two-way ANOVA followed by Sidak's multiple comparison). **(E–G)** Representative images (E) in thalamus and quantification (F) of c-Fos expression in the thalamus and cortex (G) following PTZ administration (two-tailed unpaired *t* test). Scale bar = 50 µm. Dots = mice. **(H)** Schematic of kainic acid administration. **(I)** Quantification of latency to first seizure onset (left) and incidence of seizures (right) for 3 h following kainic acid administration from four independent experiments (two-tailed unpaired *t* test). All dots represent independent mice. Data represented as mean ± SEM for bar graphs and as median ± interquartile range for violin plots. Delta: 0.5–4 Hz; Theta: 4–8 Hz; Alpha: 8–12 Hz; Sigma: 12–15 Hz; Beta: 15–30 Hz; Gamma: 30–90 Hz; High Gamma: 90–150 Hz. *P < 0.05, **P < 0.01.

Provided online are Table S1, Table S2, Table S3, Table S4, and Table S5. Table S1 shows scRNA-seq data showing differentially expressed genes per cluster. Table S2 shows genes differentially expressed in microglia after IL-33 i.c.v. vs. vehicle, in bulk RNA-seq (adjusted P value < 0.01). Table S3 shows ATAC-seq and H3K27ac ChIP-seq peaks differentially expressed in microglia after IL-33 i.c.v. vs. vehicle. Table S4 shows mEPSC and mIPSC amplitude and kinetics, and intrinsic electrical membrane properties of neurons in somatosensory thalamus of IL-33 cKO (*hGFAPCre+/−;Il33*$^{fl/fl}$) vs. littermate controls (*Il33*$^{fl/fl}$). Table S5 shows reagents and resources.